

---

# Quantum Path Computing: Computing Architecture with Propagation Paths in Multiple Plane Diffraction of Classical Sources of Fermion and Boson Particles

Burhan Gulbahar

Received: date / Accepted: date

**Abstract** Quantum computing (QC) architectures utilizing classical or coherent resources with Gaussian transformations are classically simulable as an indicator of the lack of QC power. Simple optical setups utilizing wave-particle duality and interferometers achieve QC speed-up with the cost of exponential complexity of resources in time, space or energy. However, linear optical networks composed of single photon inputs and photon number measurements such as boson sampling achieve solving problems which are not efficiently solvable by classical computers while emphasizing the power of linear optics. In this article, quantum path computing (QPC) setup is introduced as the simplest optical QC satisfying five fundamental properties all-in-one: exploiting only the coherent sources being either fermion or boson, i.e., Gaussian wave packet of standard laser, simple setup of multiple plane diffraction (MPD) with multiple slits by creating distinct propagation paths, standard intensity measurement on the detector, energy efficient design and practical problem solving capability. MPD is unique with non-Gaussian transformations by realizing an exponentially increasing number of highly interfering propagation paths while making classical simulation significantly hard. It does not require single photon resources or number resolving detection mechanisms making the experimental implementation of QC significantly low complexity. QPC setup is utilized for the solutions of specific instances of two practical and hard number theoretical problems: partial sum of Riemann theta function and period finding to solve Diophantine approximation. Quantumness of MPD with negative volume of Wigner function is numerically analyzed and open issues for the best utilization of QPC are discussed.

**Keywords** Quantum path computing · Path integral · Multi-plane diffraction · Riemann theta function · Period finding · Diophantine approximation

---

B. Gulbahar  
Department of Electrical and Electronics Engineering  
Tel.: +90-236-2330131 Fax: +90-216-5649999  
E-mail: burhan.gulbahar@ozyegin.edu.tr

## 1 Introduction

The Young's double slit experiment is at the heart of quantum mechanics (QM) with wave-particle duality as emphasized by Feynman [1]. Previous quantum computing (QC) systems utilizing classical optics, wave-particle duality or interferometer structures targeting a low complexity hardware design achieve QC speed-up for factoring problems, Gauss sum, generalized truncated Fourier sums and similar problems [2–6]. However, they have apparently the cost of exponential complexity of resources in time, space or energy making their utilization impractical for problem solving. On the other hand, more powerful architectures based on linear optics such as boson sampling achieve solving problems which are not efficiently solvable by classical computers [7]. They utilize challenging single photon sources [8, 9] and the targeted problems are not directly practical such as matrix permanents [7]. The design for a significantly low hardware complexity optical QC is a promising dream which combines all-in-one targets: a) the practical problem solving capability, b) promising QC advantages with energy efficient processing of sources and measurement not requiring exponentially increasing resources with respect to the problem size, c) using only coherent or classical particle sources including both bosons and fermions, e.g., standard laser sources with Gaussian wave packets, d) transforming the emitted source through the simple classical optics and e) intensity measurement with simple and traditional particle detectors such as photodetectors or electron detectors for photon and electron, respectively.

In this article, multi-plane diffraction (MPD) based design is proposed as a simple extension of single plane double-slit interference setup while satisfying all the required properties of the ultimate target. It utilizes a novel resource for computation, i.e., exponentially increasing number of particle propagation paths bringing an exponentially large Hilbert space in time or history in an analogical manner to multi-particle entanglement in space. MPD allows energy efficient scaling of the problem size with increased number of slits and conventional sampling of the intensities of interfering paths [10].

Feynman's history state idea [11] entangles the time steps in the computation and clock register where the simulation wave function is represented as a complex superposition of the time steps of the computation [12–14]. The entire history of QC becomes the ground state of the local Hamiltonian as a superposition entangled with time. It is utilized to show equivalence of adiabatic and gate based QC in [15]. The history state is formulated as follows [14]:

$$|\Psi_{h,0}\rangle \equiv \frac{1}{N} \sum_{i=0}^{N-1} |\Psi_{t_i,0}\rangle \equiv \frac{1}{N} \sum_{i=0}^{N-1} U_{t_i} U_{t_{i-1}} \dots U_{t_1} |\Psi_0\rangle \otimes |t_i\rangle \quad (1)$$

where  $\otimes$  is the tensor product,  $|\Psi_0\rangle$  is the initial data register state,  $|t_i\rangle$  is the clock register state and the operations  $U_{t_i}$  for  $i \in [1, N-1]$  denote  $N-1$  gates operating on the initial state. Furthermore, the clock is realized by a hopping Hamiltonian with a mapping to quantum walk (QW) as another important application of the Feynman-Kitaev construction [18]. QPC includes the states

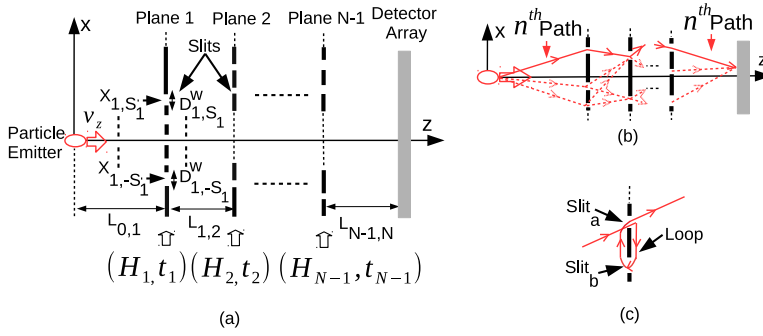


**Fig. 1** (a) QPC architecture with consecutive and parallel planes of slits, Hilbert subspaces  $(\mathcal{H}_j$  for  $j \in [0, N - 1]$ ) for the trajectories including diffraction at the event times  $t_j$ , (b)  $n^{\text{th}}$  path interfering on the sensor plane, and (c) non-classical (exotic) path making a loop between two neighbor slits [16, 17].

of the wave function at different times corresponding to the diffraction operations on each plane in an analogical manner to the entangled time steps. The propagation of the initial coherent or classical wave function is tracked as a superposition through diffractions at specific time steps allowing to model the final wave function (instead of the final Hamiltonian as in [15]) in terms of the system parameters. It requires further analysis to construct a computational relation between history state based formulation with clock registers and QPC similar to the relation realized for adiabatic computing and QWs. QPC is much more clearly modeled with consistent histories [19–21] or entangled history formulation [22, 23] of QM as thoroughly formulated in [10] where history state for the particle diffracting through planes is defined as follows:

$$|\Psi_{N-1}\rangle = \sum_n \pi_n \mathbf{P}_{N-1, n_{N-1}} \otimes \mathbf{P}_{N-2, n_{N-2}} \otimes \dots \otimes \mathbf{P}_{1, n_1} \quad (2)$$

where  $|\cdot\rangle$  is the notation introduced in [22, 23] for some history state between times  $t_1$  and  $t_{N-1}$ , the projector  $\mathbf{P}_{j,i}$  denotes the diffraction where  $i \in [-S_j, S_j]$  for the slit indices on  $j^{\text{th}}$  plane and  $\pi_n = 1$  is the equal superposition of histories (or particle trajectories) indexed by  $n$  as shown in Fig. 1. Trajectory Hilbert space is defined as follows:

$$\mathcal{H} \equiv \mathcal{H}_{N-1} \otimes \dots \otimes \mathcal{H}_1 \quad (3)$$

where  $\mathcal{H}_j$  denotes the family of the projectors  $(\mathbf{P}_{j,i})$  through  $j^{\text{th}}$  plane with slits having central positions and widths of  $X_{j,i}$  and  $D_{j,i}^w$ , respectively, where  $j \in [1, N - 1]$  and  $i \in [-S_j, S_j]$ . This provides the QC power with an entanglement relation in time domain [10] in analogy to the spatial entanglement while it is best exploited with Feynman's path integral (FPI) formulation modeling the propagation histories with a sum-over-paths approach.

Semi-classical approximation of the propagator kernel in FPI formalism is utilized to analyze classical simulability of Clifford gates on stabilizer states

and Gottesman-Knill theorem in [24]. Propagator is defined as follows [1, 24]:

$$\langle x | e^{-iHt/\hbar} | x' \rangle = \int e^{(i/\hbar)S(x, x', t)} \mathcal{D}[x(t)] \quad (4)$$

where  $\mathcal{D}[x(t)]$  is the integral over all paths and  $S(x, x', t)$  is the action for the path between  $x$  and  $x'$  evolving under Hamiltonian  $H$  at the time  $t$ . The propagator is approximated semi-classically with quadratic functional variations around the classical paths as the following [24, 25]:

$$\int e^{(i/\hbar)S(x, x', t)} \mathcal{D}[x(t)] \approx \sum_{\text{classical paths}} \mathcal{D} e^{(i/\hbar)(S + \delta^2 S / 2)} \quad (5)$$

where  $\delta S = 0$  for classical paths. In [24], it is observed for continuous systems that the propagation between Gaussian states with harmonic Hamiltonian is simulable classically by requiring only a single classical path without the importance of the relative phases of different classical contributions. The same idea is extended to the discrete case showing single path contribution for Clifford gates while requiring exponentially large number of sum-over-paths with respect to the number of qubits in case of including T gates. In addition, in [26], it is stressed out that a sum-over-paths approach for general quantum circuits includes an exponential number of terms without any efficient classical algorithm to compute this sum. The importance of interferometry architectures as a non-classicality measure is emphasized in [27] where double-slit experiment is regarded as a process to probe the phase difference between different paths. Non-classical or quantum behavior, including quantum entanglement, discord and coherence, is measured with the interferometry capability by checking whether the measurement outcome is independent of the phase information. In this article, the classical paths are hardwired to the system setup as distinct paths of propagation through slit based trajectories forcing us to calculate the phases for each path with significant interference among the paths. Intensity calculation after diffraction through consecutive planes requires the computation of exponentially increasing number of path amplitudes and phases while making the classical simulation significantly hard.

In this article, FPI based modeling of QM is preferred to characterize the effect of history for each trajectory in an easy way, i.e., the consecutive effects of the physical parameters of the diffraction slits and the travel time among the planes. FPI includes the history based formulation as an inherent element with propagation kernels more suitable to the main resource utilized for QC purposes, i.e., Hilbert space composed of the histories of the diffractive projections at specific time instants. It allows to obtain the superposition wave function easily and better formulates the exponential number of paths to compute [1]. On the other hand, it is an interesting open issue to formulate MPD with universal quantum circuit gates to understand the computational capability of MPD, e.g., testing for universal QC or modeling the group of the gates which can be implemented with QPC.

## 1.1 The Comparison with Linear Optics based Implementations

Classical simulability of linear optics implementations is achieved if the evolution of the state can be modeled in terms of a unitary matrix rather than an exponential complexity [7, 28]. Coherent state or classical inputs, e.g., Gaussian wave packet or the output of a standard laser, and adaptive Gaussian measurements are simulated in classical polynomial time since the computing system maps the original Gaussian source into Gaussian output states, e.g., with operations in Clifford semi-group [29–31]. Such states are tracked by only exploiting the mean and covariance representation of states while non-Gaussian transformations make the clever representation of Gaussian states in terms of means and variances not adequate for efficient classical simulation. Knill, Laflamme and Milburn (KLM) scheme achieves optical QC by including adaptive measurements and photon counting in addition to the simple linear optical setup [28]. Furthermore, in Boson sampling [7], single-photon inputs, which are highly challenging with the exponentially increasing difficulty of scaling for high photon numbers [8, 9], and photon number measurements are utilized which are different from the coherent Gaussian sources discussed in [29]. Modified versions of Boson sampling with Gaussian input sources and number-resolved photodetection are discussed in [32–35] introducing Gaussian version with strong evidence of classically hard simulation. They show the importance of the operations and the measurements rather than only the source for computational capabilities in a computing system.

In this article, non-Gaussian states are generated with non-Gaussian transformations, i.e., MPD, converting coherent wave packets into a superposition compared with Gaussian transformations in Clifford semi-group preserving the Gaussian nature of the wave. On the other hand, each path of the particle through slits can be simulated classically since Gaussian property is preserved for each path due to the diffraction through Gaussian slits. However, MPD requires tracking exponentially large number of classical operations since the number of propagation paths is exponentially increasing with the number of diffraction planes and the output is a superposition of these paths. Classical simulation of MPD requires exponentially increasing classical resources to track each Gaussian state in the superposition output. MPD has validity for both bosons and fermions with coherent Gaussian sources providing a significant experimental advantage compared with the difficulty to generate single photons. Besides that, it allows solutions for practical number theoretical problems including the partial sum of Riemann theta function and period finding for solutions of specific instances of Diophantine approximation problem as discussed in Sections 7 and 8. Quantumness of MPD with classical coherent sources is shown theoretically and with practical simulation parameters in [10] by violating Leggett-Garg inequality (LGI) which is the time domain analog of Bell's inequality as another supporting observation for non-classical character of QPC setup based on MPD. LGIs and Bell inequalities are utilized to test for quantumness of the systems including QC architectures.

## 1.2 Quantumness and Negative Volume of Wigner Function

Positivity of Wigner function is another indicator proposed for classicality and classical simulation of system states. Wigner function of a Gaussian state is Gaussian which is positive leading to a quasi-classical description of Gaussian inputs and Gaussian transformations. The negativity is proposed as a measure of quantum correlations including entanglement in [36–38] and as a resource for QC in [39–41]. Continuous variable Gottesman-Knill theorem is extended to a large class of non-Gaussian mixed states with positive Wigner function such that even non-Gaussian input states are not enough for QC advantages [42]. The negative volume of Wigner function is defined as follows [43]:

$$V_N \equiv \frac{1}{2} \left( \int \int |W(x, p)| dx dp - 1 \right) \quad (6)$$

where the Wigner function for the density function  $\rho$  in the one-dimensional position basis is calculated as follows:

$$W(x, p) \equiv \frac{1}{\pi} \int_{-\infty}^{\infty} \langle x + y | \rho | x - y \rangle e^{-i2\pi \frac{p}{\hbar} y} dy \quad (7)$$

In addition, negativity of Wigner function is exploited in numerous fields. An entropic parameter with quantum nature is proposed in [44] as an indicator of quantum chaos based on the negative volume of Wigner function as a non-classicality parameter. It is shown that the defined entropic parameter shows fast and large changes in the regions corresponding to classical chaos. In [45], negativity of Wigner function is utilized to detect and quantify quantum correlations in open multipartite quantum systems under the influence of both Markovian and non-Markovian environments. It is shown that the negativity is sensitive to quantum discord in these systems. In [46], it is shown that nonlinearity of a continuously driven two-level system (TLS) is enough to generate Wigner non-classical states of light by calculating Wigner function of one-dimensional and steady-state resonance fluorescence. Furthermore, the capability of the setup for generating the class of states necessary for universal quantum computing is emphasized. A rapid and coherent mechanical squeezer is introduced in [47] by utilizing four optomechanical pulses while squeezing of arbitrary mechanical inputs, including non-Gaussian states, is discussed by preserving negativity even in the presence of decoherence. They emphasize applications in quantum information technologies to enhance the storage of phononic Schrödinger cat states.

In this article, superposition of Gaussian wave packets for each trajectory of the particle has significant interference with large negative volume of Wigner function as shown in simulation studies in Section 10 with simultaneously increasing volume of the negativity and the number of propagation paths.

### 1.3 The Comparison with Quantum Walks

QW based architectures present alternative systems to the standard circuit model for QC with the speed-up of search algorithms and universal QC capability [48]. QW is considered as an extension of the classical counterpart where a walker is jumping on the sites of a lattice with a given probability [49]. The discrete and continuous QW types have the fundamental features of interference and superposition with non-classical dynamic evolution, i.e., Schrödinger dynamics of the jumper particle. An analogy between QW and multiple-slit interference architecture is proposed in [50]. Similarly, the role played by the interference effects in the dynamics of a quantum walker and simulations based on interferometric devices are discussed in [51]. There are also optical implementations of QWs resembling the structure of MPD with increasing numbers of trajectories such as multi-dimensional QWs implemented with classical optics [52–54]. Implementations of a QW on a line can be described by classical physics [55, 56]. Single photon QWs are simulated by classical coherent waves with the measurement of light intensity since single and multiple photon problems can be described with the same probability distributions [57, 58].

MPD is analogical to QW models in terms of exploiting the classical and coherent wave sources, exponentially increasing number of trajectories, interference and superposition while with the following fundamental differences:

- MPD particle covers all lattice locations (diffraction slits on the  $j$ th plane at the time  $t_j$ ) at a single time-step at once rather than adjacency based evolution. As an example, assume that a particle in a QW setup jumps to neighbor locations for a single line model. Then, there are  $\prod_{i=1}^{N-1} (2i) = 2^{N-1}(N-1)!$  paths at  $(N-1)$ th time step. Assume that the number of slits on each plane for MPD is chosen as  $2(N-1)+1$  corresponding to the maximum number of lattice sites at  $(N-1)$ th QW step. Then, the number of paths in MPD grows as  $(2N-1)^i$  at  $t_i$  compared with  $2^i i!$  in QW such that MPD has exponentially larger number of paths with an exponentially larger Hilbert space compared with the fundamental QW model.
- MPD includes the effects of exotic paths, i.e., visiting the slits on the same plane as discussed in Section 9 and as shown in Fig. 1(c), as another factor increasing the Hilbert space of MPD in an exponentially large manner.
- The model of the problems for QWs and MPD are different, e.g., ballistic expansion of the particle, exponentially faster hitting times, quantum search or graph isomorphism based problems in QW [59] compared with numerical problems related to Riemann theta functions or hidden subgroup problems in QPC by introducing a novel set of practical problems.
- There is not any coin operation in MPD to determine the next step movement. The physical properties of individual slits, i.e., the diameter and position in the proposed Gaussian slit model, combined with the history of the particle until the time of diffraction determines the probability of the particle to be diffracted through the slits on the next plane.

As a final remark, QPC proposes a setup based on coherent particle source and linear optics requiring new approaches to understand the exact nature of resources for QC advantages in a QC system. MPD has analogies with boson sampling and QWs, and promising properties in terms of sum-over-paths complexity, negativity of the Wigner function and violation of Leggett-Garg inequality in [10]. It is an open question as clearly emphasized in [60, 61] to characterize the exclusive QM properties and operations which are enhancing computing capabilities. The resources for QC are observed to be specific to the setup without allowing to simplify to a single resource or reason [3].

#### 1.4 Contributions and Main Results

The contributions in this article are summarized as follows:

1. QPC as the simplest optical QC design achieves simultaneous targets all-in-one: a) practical problem solving capability with applications for partial Riemann theta sum and period finding for solutions of specific instances of Diophantine approximation problem, b) energy efficient processing of sources and measurement, c) exploiting coherent or classical particle sources including both bosons and fermions, d) simple classical optics of MPD, and e) intensity measurement with traditional detectors.
2. QPC, for the first time, utilizes particle propagation trajectory based Hilbert space for QC purposes as a solid example of the practical utilization of history based entanglement resources.
3. Introduction and numerical simulation of a novel performance metric for the trade off between the problem complexity modeled as the number of the interfering paths and the total energy to realize interference pattern.
4. Theoretical modeling and numerical analysis of utilization of QPC for specific instances of two important and hard number theoretical problems: partial sum of Riemann theta sum and period finding for simultaneous Diophantine approximation (SDA) problem.
5. Extending single plane exotic path modeling and numerical analysis in [16, 17] to propagation through multiple planes with multiple slits.

QPC generates a black-box (BB) function  $f_{BB}[k]$  with a promising special form as thoroughly discussed in Sections 5 and 7 to utilize in solutions of important and classically hard number theoretical problems as follows:

$$f_{BB}[k] \equiv \left| \sum_{x_1 \in X_1} \dots \sum_{x_{N-1} \in X_{N-1}} e^{(A_x + \iota B_x)(k T_s)^2} \Upsilon_x e^{\vec{x}^T \mathbf{H}_x \vec{x}} e^{(\vec{h}_x^T \vec{x}) k T_s} \right|^2 \quad (8)$$

where  $k \in \mathbb{Z}$ ,  $T_s \in \mathbb{R}^+$  is a sampling interval,  $A_x \in \mathbb{R}^-$ ,  $B_x \in \mathbb{R}^+$ ,  $\Upsilon_x \in \mathbb{C}$ ,  $\vec{x} = [x_1 \ x_2 \ \dots \ x_{N-1}]^T$  is a column vector composed of the slit positions  $x_j$  on each  $j$ th plane chosen from the corresponding set  $X_j$  with a countable number of elements. The complex valued matrix  $\mathbf{H}_x \equiv \mathbf{H}_{R,x} + \iota \mathbf{H}_{I,x}$  and



the vector  $\vec{h}_x \equiv \vec{c}_x + i\vec{d}_x$  of the system setup have the values depending on the slit widths on each  $j$ th plane for  $j \in [1, N - 1]$  corresponding to the specific selection of slits in the path  $\vec{x}$ , inter-plane durations for the particle propagation, particle mass  $m$ , beam width  $\sigma_0$  of the Gaussian source wave packet and Planck's constant  $\hbar$ . Each selection of the slits in  $\vec{x}$  corresponds to a unique path for the particle to diffract. Therefore, the positions of the slits identify the index of a particular path or trajectory. In this article, the computational hardness of calculating (8) in an efficient manner is discussed and two different methods utilizing (8) for practical problems are introduced.

The first method exploiting QPC calculates partial sum of Riemann theta function or multi-dimensional theta function as modeled in detail in Section 7 with important applications in number theory and geometry [62–67]. If the slit widths on each plane are constrained as being uniform specific to each plane, then the parameters  $A, B, \Upsilon, \mathbf{H}$  and  $\vec{h}$  in (8) become independent of the specific path  $\vec{x}$ . Then, BB function is converted to a form of partial sum of Riemann theta function. The first utilization of QPC is to prepare a setup to solve specific groups of Riemann theta functions. Riemann theta function has important computational difficulties requiring complicated methods for the large number of contributions in the summation growing exponentially with  $N$ . Therefore, the more complicated form in (8) with matrix and vector parameters depending on the path  $\vec{x}$  has a much harder computational complexity. There is no apparent way of computing (8) in a classically efficient manner for the specific sets of the matrices and vectors corresponding to a general experimental MPD setup with the user determined system parameters.

The second solution method based on QPC utilizes the phase in  $e^{(\vec{h}_x^T \vec{x}) k T_s} = e^{(\vec{c}_x^T \vec{x}) k T_s} e^{i(\vec{d}_x^T \vec{x}) k T_s}$  for period finding and the solution of specific instances of SDA problems. QPC period finding algorithm is introduced in Section 8 in analogy to QC period finding based on quantum gates [68]. Exponentially growing number of different  $b[n] \in \mathbb{R}$  values are obtained with the multiplication  $b[n] \propto \vec{d}_x^T \vec{x}$  varying for each path  $\vec{x}$  indexed with  $n$  as a classically hard SDA problem. Simple and classically solvable versions obtained with  $b[n] \propto \vec{d}^T \vec{x}$  with path independent  $\vec{d}$  are numerically analyzed to understand the main idea in QPC based period finding.

In addition, a novel performance metric is introduced by emphasizing the trade off between the required number of particles or the amount of energy sources to accurately compute  $f_{BB}[k]$  for solving a specific problem and the number of interfering paths. The non-classical properties of MPD is further analyzed and simulated by calculating the negative volume of Wigner function in comparison with the logarithmic number of the propagation paths.

Some open issues are discussed. It is an open issue to find the sets of SDA problems which can be solved with an energy efficient QPC setup. Furthermore, designing the optimum algorithm to perform period finding in analogy to QC period finding algorithms utilizing continued fractions and inverse fast Fourier transform (IFFT) is an open issue [68]. Moreover, determining whether the problems whose solutions can be efficiently provided with QPC can also

be efficiently solved with classical computers is another important open issue. Formal complexity analysis of the QPC power obtained with (8) is an open issue. Besides that, it is an open issue to design a novel multiple time diffraction setup with different geometries rather than simple planar diffractions in a manner tuned to a specific target problem. On the other hand, the modeling of BB function for the setups with arbitrary slits is an open issue compared with the Gaussian slit assumption in the article. The extension to arbitrary slits results in the solutions of different computational problems.

### 1.5 Methodology

Exponentially increasing number of interfering trajectories or paths are utilized to define a novel resource for QC, i.e., Hilbert space of the particle propagation trajectories. A novel computing solution denoted by QPC is defined by exploiting two special novel features:

1. Consecutive and parallel diffraction planes with multiple slits creating exponentially large number of particle trajectories until being detected on the final plane, i.e., sensor plane, creating tensor product Hilbert subspaces of diffraction through each plane. Calculation of the exact intensity distribution on each plane requires exponentially increasing number of path integrals or summations making the classical simulation significantly difficult. It is valid for both bosons and fermions including electrons, photons, neutrons and even molecules. The particle source is assumed to be a Gaussian wave packet as the coherent or classical output of a standard laser.
2. Computation capability of the special BB function in (8) or (14) as the main computing power of the system design. Energy-complexity trade off is analyzed based on the number of required summations of the paths on the sensor plane compared with the total probability of the measurement. Increasing number of slits with closely spaced spatial intervals results in an increase in both the complexity and the probability of the measurement as a unique power and advantage of MPD design.

There is not any measurement regarding a specific trajectory but only interference pattern on the final plane without violating standard QM. Interference experiments are recently getting more attention to analyze non-classical (exotic) paths, e.g., passing through the slits on the same plane consecutively and even multiple times as shown in Fig. 1(c), and Gouy phase effect in the measurement of Sorkin parameter [16, 17]. QPC extends, for the first time, previous formulation to MPD setups while simulating the effects of multiple exotic paths on multiple planes compared with previous studies utilizing single plane based diffraction and single exotic path [16, 17].

## 1.6 Organization

In Section 2, physical setup is presented. In Sections 3 and 4, trajectory Hilbert space and MPD modeling with FPIs are presented, respectively. QPC BB function and the computational hardness are discussed in Section 5. Energy flow versus complexity trade off is modeled in Section 6. In Sections 7 and 8, the application of QPC for partial sum of Riemann theta function and period finding are presented, respectively. In Section 9, effects of non-classical paths are modeled while in Section 10, numerical simulations are performed. Finally, in Sections 11 and 12, open issues and conclusions are presented, respectively.

## 2 Multi-plane Diffraction System Design

There are  $N - 1$  planes of slits in front of a particle source and the interference pattern is observed by the sensor plane with the index  $N$  as shown in Fig. 1(a). Particles are assumed to perform free space propagation between the planes. The plane with the index  $j$  has in total  $S_{j,T} \equiv 2S_j + 1$  slits with  $(\cdot)_{j,T}$  representing the total and  $S_j$  is utilized to index the slits with the numbers between  $-S_j$  and  $S_j$ . The central positions and widths of slits are given by  $X_{j,i}$  and  $D_{j,i}^w$ , respectively, where  $j \in [1, N-1]$  and  $i \in [-S_j, S_j]$ . The set of ordered slit positions on  $j$ th plane is denoted by the column vector  $\vec{X}_j$  or with the set denoted by  $X_j$ . Row vectors are represented with the transpose operation, i.e.,  $(\cdot)^T$ . The whole set of slit positions on  $N - 1$  parallel planes are denoted by  $\mathbf{X}_{N-1}$ . Distance between  $i$ th and  $j$ th planes is given by  $L_{i,j}$  where the distances from particle emission source to the first plane and from  $(N - 1)$ th plane to the detection plane are given by  $L_{0,1}$  and  $L_{N-1,N}$ , respectively. Behavior of the particle is assumed to be classical in  $z$ -axis with the velocity given by  $v_z$  while quantum superposition interference is assumed to be observed in  $x$ -axis as a one dimensional model to be easily extended to two dimensional (2D) systems.

Time duration for the particle to travel between  $(j - 1)$ th and  $j$ th planes is assumed to be  $t_{j-1,j} = L_{j-1,j} / v_z$  for  $j \in [1, N]$ . Position in  $x$ -axis on  $j$ th plane is denoted by  $x_j$  while the wave functions of  $n$ th path and superposition of all paths on  $j$ th plane are denoted by  $\Psi_{n,j}(x_j)$  and  $\Psi_j(x_j)$ , respectively. Inter-plane distance and duration vectors are represented by  $\vec{L}^T = [L_{0,1} \dots L_{N-1,N}]$  and  $\vec{t}^T = [t_{0,1} \dots t_{N-1,N}]$ , respectively. Trajectories are indexed by  $n$  for  $n \in [0, N_p - 1]$  as shown in Fig. 1(b) where  $N_p = \prod_{j=1}^{N-1} S_{j,T}$  is the total number of paths until to the sensor plane ( $N$ th plane) measurement and  $Path_n \equiv \{s_{n,1}, s_{n,2}, \dots, s_{n,N-1}; s_{n,j} \in [-S_j, S_j]\}$  is the indices of the slits for  $n$ th path. Therefore, slit position for  $n$ th path on  $j$ th plane is given by  $X_{j,s_{n,j}}$ . Similarly,  $N_{p,j} \equiv \prod_{i=1}^{j-1} S_{i,T}$  denotes the number of paths for the particle diffracting through the  $j - 1$ th plane.

Calculation of inter-plane durations by  $t_{j-1,j} = L_{j-1,j} / v_z$  is accurate due to  $L_{j-1,j} \gg D_{j-1,i}^w, X_{j-1,i}$  for  $j \in [2, N]$  and  $i \in [-S_{j-1}, S_{j-1}]$  such that quantum effects are emphasized in  $x$ -axis. Non-relativistic modeling of particle

behavior is assumed. Source is a single Gaussian wave function while Gaussian slits are utilized with FPI approach [1]. Next, trajectory Hilbert space as the resource for QPC is described.

### 3 Trajectory Hilbert Space

QPC realizes subspaces analogical to spatial qudits such that diffractive projection family through the set of the slits on  $j$ th plane results in a Hilbert subspace at  $t_j$  as shown in Fig. 1(a). There is not any measurement to determine the diffracted slit positions in any trajectory. It does not violate the standard interpretation of QM while utilizing superposition of trajectories with a tensor product space of diffraction events [19]. FPI methodology results in the intensity measurement  $I_N(x) = \left| \sum_{n=0}^{N_p-1} \Psi_{n,N}(x) \right|^2$  on  $N$ th plane as follows:

$$I_N(x) = \left| \sum_{n=0}^{N_p-1} \int_{\vec{x}} K_n(x, \vec{x}; t_N, t_{N-1}, \dots, t_0) \Psi_0(x_0) d\vec{x} \right|^2 \quad (9)$$

where  $t_0$  and  $t_N$  are initial and the measurement times, respectively,  $t_j$  for  $j \in [1, N-1]$  is the diffraction time,  $x_0$  and  $x$  are the initial and the sensor plane position variables, respectively,  $\Psi_0(x)$  is the coherent source wave function,  $\Psi_{n,N}(x)$  is the wave function of  $n$ th trajectory on the sensor plane,  $\int_{\vec{x}} d\vec{x}$  denotes the integration with respect to  $x_j$  for  $j \in [0, N-1]$  and  $K_n(x, \vec{x}; t_N, t_{N-1}, \dots, t_0) = K_n(x, x_{N-1}, \dots, x_0; t_N, t_{N-1}, \dots, t_0)$  is the overall propagation kernel with the detailed models defined in Section 4.

The trajectory of the particle is defined as a sequence of projection operators corresponding to the diffraction through slits. Consecutive set of slits for  $n$ th trajectory is defined as  $S \rightarrow X_{1,s_{n,1}} \rightarrow X_{2,s_{n,2}} \rightarrow \dots \rightarrow X_{N-1,s_{n,N-1}}$  where  $S$  is the initial state at the source at  $t_0$ . Trajectory Hilbert space is defined in (3) in Section 1. Therefore, as the particle passes through multiple planes, each possible trajectory results in an interfering functional contribution on the final wave function on the sensor plane. Projection operators denoting the particle to be in the Gaussian slit (for a one dimensional model for simplicity) are defined in a coarse grained sense as discussed in [69] as follows:

$$P_{\beta_{j,i}}(X_{j,i}) \equiv \int_{-\infty}^{\infty} dx \exp\left(-\frac{(x - X_{j,i})^2}{2\beta_{j,i}^2}\right) |x\rangle \langle x| \quad (10)$$

where the effective slit width is  $D_{j,i}^w \equiv 2\beta_{j,i}$ ,  $j \in [1, N-1]$  and  $i \in [-S_j, S_j]$ . If the slit widths are uniform for each  $j$ th plane with  $\beta_j$ , then  $\vec{\beta} \equiv [\beta_1, \dots, \beta_{N-1}]^T$  represents the vector of the slit widths. If the slit widths are different, then  $S_\beta$  denotes the set with the elements  $\beta_{j,i}$ . The set of Gaussian slit projectors satisfies mutual exclusivity in an approximate sense since the integrals include intersections of slit intervals defined by the widths  $\beta_{j,i}$ . In simulations, slit distances are chosen large enough to satisfy  $\exp(-(X_{j,m} - X_{j,l})^2 / (2\beta_{j,m}^2)) \ll 1$  for  $m \neq l$ . Next, FPI modeling of MPD is presented.

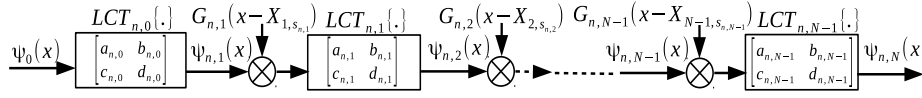


**Fig. 2** Evolution of  $\Psi_0(x)$  in  $n$ th path as consecutive operations of  $LCT_{n,0}\{\cdot\}$  followed by the operations of  $LCT_{n,j}\{\cdot\}$  and multiplication by the effective slit functions  $G_{n,j}(x_j)$  for  $j \in [1, N-1]$  resulting in the final wave function of  $\Psi_{n,N}(x)$ .

#### 4 Multi-plane Diffraction Modeling

$\Psi_{n,N}(x)$  is calculated with free particle kernels [1].  $K(x_1, t_1; x_0, t_0)$  denotes free particle kernel for the paths between time-position values  $(t_0, x_0)$  and  $(t_1, x_1)$  defined as follows:

$$K(x_1, t_1; x_0, t_0) = \sqrt{m/(2\pi i \hbar \Delta t)} \exp(i m \Delta x^2 / (2 \hbar \Delta t)) \quad (11)$$

where  $\Delta t = t_1 - t_0$  and  $\Delta x = x_1 - x_0$  and  $m$  is the free particle mass. If  $\int_{\vec{x}} d\vec{x}$  denotes the integration with respect to  $x_j$  for  $j \in [0, N-1]$  between  $-\infty$  and  $\infty$ , then  $\Psi_{n,N}(x)$  is given as follows by describing  $K_n(\cdot)$  in (9):

$$\int_{\vec{x}} d\vec{x} K(x, t_N; x_{N-1}, t_{N-1}) G_{n,N-1}(x_{N-1} - X_{N-1, s_{n,N-1}}) \left( \prod_{j=1}^{N-2} K(x_{j+1}, t_{j+1}; x_j, t_j) G_{n,j}(x_j - X_{j, s_{n,j}}) \right) K(x_1, t_1; x_0, t_0) \Psi_0(x_0) \quad (12)$$

where  $t_j = t_0 + \sum_{k=1}^j t_{k-1, k}$  for  $j \in [0, N]$  and  $G_{n,j}(x_j)$  denotes the effective function of the slit with the index  $s_{n,j}$  on  $j$ th plane for  $n$ th path. The result is described in terms of linear canonical transforms (LCTs). LCT of a function  $f(x)$ , i.e.,  $LCT_{a,b,c,d}\{f(x)\}$ , is defined as  $\exp\{-i\frac{\pi}{4}\} \sqrt{\eta} \int_{-\infty}^{\infty} \exp\{i\pi(\alpha x^2 - 2\eta x u + \gamma u^2)\} f(u) du$  where LCT matrix is  $\{a, b, c, d\} \equiv \{\gamma/\eta, 1/\eta, (\alpha\gamma - \eta^2)/\eta, \alpha/\eta\}$  and  $ad - bc = 1$  for a given set of parameters  $(\alpha, \gamma, \eta)$  [70]. Then, evolution of  $\Psi_0(x_0)$  is represented as shown in Fig. 2 where  $LCT_{n,j}\{\cdot\}$  denotes the LCT with the matrix  $\{a_{n,j}, b_{n,j}, c_{n,j}, d_{n,j}\} \equiv \{1, 2\pi\hbar t_{j,j+1}/m, 0, 1\}$  with the transformation parameters  $\alpha = \gamma = \eta = m/(2\pi\hbar t_{j,j+1})$  for  $j \in [0, N-1]$  not depending on the path index  $n$  due to the classical approximation in  $z$ -axis. Next, QPC BB function and its computational hardness are discussed.

#### 5 Quantum Path Computing Black Box Function and Computational Hardness

Interference on sensor plane is transformed into a form to exploit quantum superposition and computation of BB function for performing QC tasks. For simplicity of calculation, we firstly assume that the slit widths are the same on a single plane, i.e.,  $G_{n,j}(x) = \exp(-x^2/(2\beta_j^2))$  with  $D_{j,i}^w \equiv 2\beta_j$  for  $j$ th plane. Then, it is extended to a general MPD setup with different slit widths, i.e.,  $D_{j,i}^w \equiv 2\beta_{j,i}$ . The source wave function is a Gaussian wave packet of the form  $\Psi_0(x) = \exp(-x^2/(2\sigma_0^2))/\sqrt{\sigma_0}\sqrt{\pi}$  [1, 16]. Then, after taking the

consecutive path integrals of  $\Psi_0(x)$  through each path as shown in Appendix A, the following superposition intensity  $I_N(x)$  is obtained:

$$I_N(x) = e^{2A_{N-1}x^2} \left| \sum_{n=0}^{N_p-1} \Upsilon_N e^{\vec{x}_n^T \mathbf{H}_R \vec{x}_n} e^{i \vec{x}_n^T \mathbf{H}_I \vec{x}_n} e^{\vec{c}^T \vec{x}_n x} e^{i \vec{d}^T \vec{x}_n x} \right|^2 \quad (13)$$

where  $\mathbf{H} = \mathbf{H}_R + i \mathbf{H}_I$  is  $N-1 \times N-1$  matrix which is composed of correlated real  $\mathbf{H}_R$  and imaginary parts  $\mathbf{H}_I$ ,  $A_{N-1}$  is a real negative variable,  $\Upsilon_N$  is a complex variable,  $\vec{c}$  and  $\vec{d}$  are  $N-1$  dimensional column vectors, and the slit position vector for  $n$ th trajectory is  $\vec{x}_n \equiv [X_{1,s_{n,1}} \dots X_{N-1,s_{n,N-1}}]^T$ . The parameters  $\Upsilon_N$ ,  $\mathbf{H}$ ,  $\vec{c}$ ,  $\vec{d}$  and  $A_{N-1}$  depend on  $\vec{\beta}$ , inter plane duration vector  $\vec{t}$ , the source parameter  $\sigma_0$ , Planck's constant  $\hbar$  and particle mass  $m$ . They do not depend on trajectory index  $n$  or  $\vec{x}_n$  due to the assumption of uniform slit widths. The relaxation of uniform slit widths results in trajectory dependent parameter sets as shown next. The combined design of  $\vec{x}_n$ ,  $\Upsilon_N$ ,  $\mathbf{H}$ ,  $\vec{c}$ ,  $\vec{d}$  and  $A_{N-1}$  while choosing adapted set of  $x$ -axis samples promises a solution to optimization problems with significantly large  $N_p$ .

If the constraint of the uniform slit width on each plane is relaxed, then  $\Upsilon_N$ ,  $\mathbf{H}$ ,  $\vec{c}$ ,  $\vec{d}$  and  $A_{N-1}$  will all depend on the path index  $n$  since there is a consecutive set of different  $\beta_{j,i}$  values along each path effecting the final output value. If the new parameters depending on  $n$  are denoted with  $A_{N-1,n}$ ,  $B_{N-1,n}$ ,  $\Upsilon_{N,n}$ ,  $\mathbf{H}_{N-1,n} \equiv \mathbf{H}_{R,N-1,n} + i \mathbf{H}_{I,N-1,n}$ ,  $\vec{c}_{N-1,n}$  and  $\vec{d}_{N-1,n}$ , then the general form of the output intensity denoted by  $I_N^G(x)$  is given as follows:

$$I_N^G(x) = \left| \sum_{n=0}^{N_p-1} \left( e^{(A_{N-1,n} + i B_{N-1,n})x^2} \Upsilon_{N,n} e^{\vec{x}_n^T \mathbf{H}_{R,N-1,n} \vec{x}_n} \times e^{i \vec{x}_n^T \mathbf{H}_{I,N-1,n} \vec{x}_n} e^{\vec{c}_{N-1,n}^T \vec{x}_n x} e^{i \vec{d}_{N-1,n}^T \vec{x}_n x} \right) \right|^2 \quad (14)$$

$I_N^G(x)$  has a much more complicated form without any apparent and efficient classical way to calculate compared to the approximation methods of Riemann theta function in (13) which is already extremely hard to calculate classically. The matrices  $\mathbf{H}_{N-1,n}$  changing for each trajectory make the problem significantly difficult. It is an open issue whether there exists a polynomial complexity solution to calculate  $I_N^G(x)$  by exploiting the correlation among  $\Upsilon_{N,n}$ ,  $\mathbf{H}_{N-1,n}$ ,  $\vec{c}_{N-1,n}$ ,  $\vec{d}_{N-1,n}$ ,  $A_{N-1,n}$  and  $B_{N-1,n}$  for the hardest case of non-uniform slit widths and non-uniform slit position space including the path vectors  $\vec{x}_n$  obtained from  $X_{j,i}$  where  $j \in [1, N-1]$  and  $i \in [-S_j, S_j]$ . In Section 9, the effects of exotic paths are modeled which requires further modification of (14) to include exotic paths making the classical calculation much harder.

It is an open issue to determine the complexity class of calculating (13) and (14) with classical and universal quantum computers. Another open issue

is to determine the best method to utilize (13) and (14) for computational power and solving appropriate numerical problems. In Sections 7 and 8, the solutions for partial sum of Riemann theta function (Chapter 8 in [66]) and period finding type solution for HSPs [68] are provided as examples. Next, a performance metric is defined for the trade off between energy and complexity.

## 6 Energy Flow and Complexity

Although Hilbert space of the paths enlarges exponentially, the total number of large amplitude paths is smaller than the total number of possible paths as numerically analyzed in Section 10. The probability of detection decreases as the particle forwards. There is a trade off between the particle energy and the computational complexity (approximated as the number of paths required to be calculated). Magnitude of  $n$ th path on  $j$ th plane is defined as follows:

$$I_{path}(n, j) \equiv \sum_{k=-\infty}^{\infty} T_s |\Psi_{n,j}(k T_s)|^2 \quad (15)$$

The trade off provides a better representation of interference based Hilbert space as the number of planes increases. Many paths contribute little to a specific sampling position  $k T_s$  while a large number of them should be taken into account to calculate the final intensity. A performance metric for path magnitude based dimension ( $D_j(\epsilon)$ ) and the probability of detection ( $P_j$ ) denoted by  $[D_j(\epsilon), P_j]$  is defined as follows:

$$D_j(\epsilon) : \text{count of } n \text{ where } I_{path}(n, j) > \epsilon I_{path}^{max}(n, j),$$

$$P_j \equiv \sum_{k=-\infty}^{\infty} T_s I_j(k T_s) \quad (16)$$

where  $I_{path}^{max}(n, j) \equiv \max_{n \in [0, N_{p,j}-1]} \{I_{path}(n, j)\}$ , and  $P_j$  and  $I_j(x_j)$  are probability to be detected and intensity on  $j$ th plane, respectively. The number of paths effective on  $j$ th plane increases as  $\epsilon < 1$  decreases while  $\epsilon = 0$  gives the total number of paths  $N_{p,j}$ . The definition in (16) proposes an interference based and energy constrained Hilbert space where  $D_j(\epsilon) \times P_j$  is a novel performance metric. The intensity is normalized with FPI modeling, i.e.,  $P_0 = P_1 = 1$ .

Different sampling points on the sensor plane require different sets of paths in the summation as shown in numerical analysis in Section 10. Therefore, reliable value of  $\epsilon$  changes with respect to  $k T_s$  while  $\epsilon = 0$  could be taken the most reliable value forcing the calculation of all the paths for the complete intensity waveform on the sensor plane. The effects of the paths are analyzed by defining three different cumulative summation methods of the path wave functions with indices sorted with different mechanisms.  $I_{j,s}^a(k T_s)$  and  $I_{j,s}^b(k T_s)$  denote the cumulative sum intensities by summing the contributions from the paths indexed by sorting with respect to the descending magnitude of the

total probability of the path on the layer and the descending magnitude of the path wave function at the sampling point  $kT_s$ , respectively. Therefore,  $I_{j,s}^b(kT_s)$  has a local characteristics tuned to the sampling point.  $I_{j,s}^c(kT_s)$  denotes the cumulative sum with the paths indexed by sorting with respect to the paired trajectories almost canceling each other. In other words, the paths are firstly sorted with respect to descending magnitude of the wave functions at the sampling point  $kT_s$  providing the first sorting outcome. Then, the first path is taken (index of  $\Psi_{n,j}(kT_s)$  starting from  $n = 1$  instead of  $n = 0$ ) and a search is performed among the remaining paths for minimizing  $|\Psi_{1,j}(kT_s) + \Psi_{m,j}(kT_s)|^2$  and a new index of 2 is given to the path with the index  $m$  which almost cancels the wave function of the first path. Then, the next path in the first sorting outcome is taken and consecutive searches are made for each path with the same manner. In this method, we check whether there are specific groups of paths directly canceling each other. However, even if the paths cancel each other, it could be extremely hard to couple the paths among the exponentially large number of trajectories. As a result, the paths are indexed with three different sorting methods denoted with the indices  $n_a$ ,  $n_b$  and  $n_c$  where the respective cumulative intensities until the path with the index  $n_f \leq N_{p,j}$  are defined as follows:

$$I_{j,s}^{type}(n_f, kT_s) \equiv \left| \sum_{n_{type}=1}^{n_f} \Psi_{n_{type},j}(kT_s) \right|^2 \quad (17)$$

where *type* denotes *a*, *b* or *c*. Observe that all the sorting types sort the paths with respect to the descending order of the magnitudes. Next, two different methods for exploiting QPC in number theoretical problems are described.

## 7 QPC Solution-1: Partial Sum of Riemann Theta Function

The Riemann theta function designed by Riemann [63] generalizes Jacobi's theta functions of one variable [71] to solve the Jacobi inversion problem [62, 64]. It has important applications in geometry, arithmetic and number theory including the theory of partition functions, representation of integers, evaluation of infinite formal products and modular forms [64], nonlinear spectral theory for water wave dynamics and oceanography [66], nonlinear Fourier analysis [67], conformal field theories, partial differential equations and cryptography [65]. Theta function in  $N - 1$  dimensions is defined as follows [62]:

$$\Theta(\mathbf{Y}, \vec{y}) \equiv \sum_{a_1 \in \mathbb{Z}} \dots \sum_{a_{N-1} \in \mathbb{Z}} e^{-\pi \vec{a}^T (\mathbf{Y}_R + \imath \mathbf{Y}_I) \vec{a} + 2\pi (\vec{y}_R^T + \imath \vec{y}_I^T) \vec{a}} \quad (18)$$

where  $\vec{a}^T = [a_1 \ a_2 \ \dots \ a_{N-1}]$ ,  $\mathbf{Y} \equiv \mathbf{Y}_R + \imath \mathbf{Y}_I$ ,  $\mathbf{Y}_R$  is a positive definite and symmetric real matrix,  $\mathbf{Y}_I$  is a real symmetric matrix,  $\vec{y} \equiv \vec{y}_R^T + \imath \vec{y}_I^T$ ,  $\vec{y}_R$  and  $\vec{y}_I$  are real vectors. The positive definiteness of  $\mathbf{Y}_R$  satisfies the convergence of the infinite summation. There are various methods utilized to



approximate the series by utilizing partial summation of theta function defined by limiting the bounds as follows:

$$\Theta_M(\mathbf{Y}, \vec{y}) \equiv \sum_{a_1=-M}^M \dots \sum_{a_{N-1}=-M}^M e^{-\pi \vec{a}^T (\mathbf{Y}_R + \imath \mathbf{Y}_I) \vec{a} + 2\pi (\vec{y}_R^T + \imath \vec{y}_I^T) \vec{a}} \quad (19)$$

It is exponentially hard to find the summation in (19) with the brute force method on  $N - 1$  dimensional cubic lattice space of  $\vec{a}$  as thoroughly discussed in [66]. Approximation methods satisfying special conditions are presented in [62,66] with Fourier analysis and the summation over lattice spaces of spherical or ellipsoidal volumes. Therefore, calculation of Riemann theta functions is a significant challenge as an important number theoretical problem.

The superposition wave function in (13) is easily converted to Riemann theta function by choosing slit positions on a plane in a periodic manner and with the constraint of uniform slit width specific to each plane. If  $S_j = M$ ,  $X_{j,i} = a_j \Delta x_j$  for  $j \in [1, N - 1]$  and  $a_j \in [-M, M]$  and  $x = k T_s$ , then (13) is transformed into  $e^{2 A_{N-1} k^2 T_s^2} |\Upsilon_N|^2 \tilde{I}_N^R(x)$  where  $\tilde{I}_N^R(x)$  becomes the following:

$$\tilde{I}_N^R(x) = \left| \sum_{a_1=-M}^M \dots \sum_{a_{N-1}=-M}^M e^{-\pi \vec{a}^T \tilde{\mathbf{Y}} \vec{a}} e^{2\pi \vec{y}^T \vec{a}} \right|^2 = |\Theta_M(\tilde{\mathbf{Y}}, \vec{y})|^2 \quad (20)$$

where  $\tilde{\mathbf{Y}} \equiv -\mathbf{D}\mathbf{H}\mathbf{D} / \pi$ ,  $\vec{y} \equiv x \mathbf{D} (\vec{c} + \imath \vec{d}) / (2\pi)$  and  $\mathbf{D}$  is the diagonal matrix with the diagonal elements formed of  $\{\Delta x_1, \Delta x_2, \dots, \Delta x_{N-1}\}$ . The quadratic form of  $\vec{a}^T \tilde{\mathbf{Y}} \vec{a}$  allows the calculation with a symmetric matrix by converting  $\tilde{\mathbf{Y}}$  with  $\tilde{\mathbf{Y}}_s \equiv (\tilde{\mathbf{Y}} + \tilde{\mathbf{Y}}^T) / 2$ . As a result, QPC setup is utilized to calculate the amplitudes of the specific Riemann theta functions with the matrix and vector input parameters defined by  $\tilde{\mathbf{Y}}_s$  and  $\vec{y}$ , respectively.

On the other hand, QPC performs more complicated functions compared to Riemann theta function including the summation over irrational and non-uniform sampling grid  $a_j$  for  $j \in [1, N - 1]$  compared to the integer and periodic grid of the sampling points. Furthermore, transforming the general wave function  $I_N^G(x)$  with non-uniform slit widths results in a special form of Riemann theta function having different parameters  $\tilde{\mathbf{Y}}_s$  and  $\vec{y}$  for each point on the summation grid. This problem has not any practical and visible method to practically calculate in polynomial time complexity with classical computers. It is an open issue to analyze whether there are classically efficient methods to compute the Riemann theta functions obtained with  $\tilde{I}_N^R(x)$  and  $I_N^G(x)$ . Next, the phases of the defined wave forms are utilized for period finding type solutions for specific SDA problems.

## 8 QPC Solution-2: Period Finding

An analogy is presented with QPC based solution and the period finding algorithms in traditional QC algorithms exploiting superposition and entangle-

ment together to realize quantum Fourier transform (QFT). A special function  $f_n(\vec{x})$  is defined with periodicity property. The analogy between tensor product spaces of trajectories and multiple particle entanglement resources is described in Table 1. Intensity is sampled as follows:

$$\begin{aligned} I_N^G[k] &\equiv \left| \sum_{n=0}^{N_p-1} e^{(A_{N-1,n} + i B_{N-1,n}) (k T_s)^2} \Upsilon_{N,n} \right. \\ &\quad \left. e^{\vec{x}_n^T \mathbf{H}_{R,N-1,n} \vec{x}_n} e^{\vec{d}_{N-1,n}^T \vec{x}_n k T_s} e^{i \Theta[n,k]} \right|^2 \quad (21) \\ &= \left| \sum_{n=0}^{N_p-1} \gamma_{f,n} \left( \frac{T_s}{2\pi} \vec{x}_n, k \right) f_n \left( \frac{k T_s}{2\pi} \vec{x}_n \right) \right|^2 \end{aligned}$$

where  $x = k T_s$  for integer indices  $k \in [-\infty, \infty]$  and sampling period  $T_s$ , and  $\Theta[n, k]$ ,  $\gamma_{f,n}(\vec{x}, k)$  and  $f_n(\vec{x})$  depending on the physical properties of the specific QPC setup are defined as follows:

$$\Theta[n, k] \equiv \vec{x}_n^T \mathbf{H}_{I,N-1,n} \vec{x}_n + \vec{d}_{N-1,n}^T \vec{x}_n k T_s \quad (22)$$

$$\begin{aligned} \gamma_{f,n}(\vec{x}, k) &\equiv e^{(A_{N-1,n} + i B_{N-1,n}) (k T_s)^2} \Upsilon_{N,n} \\ &\quad e^{(4\pi^2 / T_s^2) \vec{x}^T \mathbf{H}_{N-1,n} \vec{x}} e^{2\pi \vec{d}_{N-1,n}^T \vec{x} k} \quad (23) \end{aligned}$$

$$f_n(\vec{x}) \equiv e^{i 2\pi \vec{d}_{N-1,n}^T \vec{x}} \quad (24)$$

The analogy between QC (Section 5.4.1 in [68]) and QPC period finding is shown in Table 1 and described in detail after defining the following problems:

**Problem 1 Periodicity detection:** Find the minimum integer  $\tilde{k} \in \mathbb{Z}^+$  scaling the given set of  $N-1$  dimensional real vectors  $\vec{d}_{N-1,n}$  for a given **non-uniform lattice** denoted by  $\mathbf{X}_{N-1}^s$  resulting in a **reciprocal integer lattice** denoted by  $\Lambda$  by minimizing the error term  $\epsilon_n$  for  $n \in [0, N_p - 1]$  in a defined average sense such that  $\Lambda \equiv \{\tilde{k} \vec{d}_{N-1,n}^T \vec{x}_n^s + \epsilon_n \in \mathbb{Z}; \forall \vec{x}_n^s, n \in [0, N_p - 1]\}$  where  $\mathbf{X}_{N-1}^s$  formed of a set of real vectors  $\vec{x}_n^s$  is defined as follows:

$$\begin{aligned} \vec{x}_n^s &\equiv (2\pi)^{-1} T_s [\vec{x}_n(1) \dots \vec{x}_n(N-1)] \text{ with } \vec{x}_n(j) \in \{X_{j,-S_j}, \dots, X_{j,S_j}\} \\ &\quad \text{s.t. } X_{j,i} - X_{j,i+1} > 2\alpha \max\{\beta_{j,i}, \beta_{j,i+1}\}; N \geq 2; \alpha \geq 1 \\ &\quad \text{where } n \in [0, N_p - 1]; j \in [1, N - 1]; i \in [-S_j, S_j] \\ &\quad S_j, N \in \mathbb{Z}^+; \beta_{j,i}, T_s, \alpha \in \mathbb{R}^+; X_{j,i} \in \mathbb{R} \quad (25) \end{aligned}$$

where  $N_p \equiv \prod_{j=1}^{N-1} (2S_j + 1)$ , and  $\mathbb{Z}$ ,  $\mathbb{Z}^+$ ,  $\mathbb{R}$  and  $\mathbb{R}^+$  are the sets of integers, positive integers, real and positive real values, respectively.

The condition  $X_{j,i} - X_{j,i+1} > 2\alpha \max\{\beta_{j,i}, \beta_{j,i+1}\}$  for large  $\alpha$  satisfies Gaussian slit property. The others define the physical setup described in Sections 2 and 4. SDA problem presented in [72] is analogical and defined as follows:

**Problem 2 SDA:** *Decide the existence and find the minimum integer  $\tilde{k} \in \mathbb{Z}^+$  where  $\tilde{k} \leq K_{pre}$  for some pre-defined  $K_{pre} \in \mathbb{Z}^+$  such that it is SDA solution for the set of real numbers in the set  $S_b = \{b_0, b_1, \dots, b_{N_p-1}\}$  satisfying the relation  $|\tilde{k}b[n] - k_n| < \epsilon$  for  $n \in [0, N_p - 1]$  and for some  $k_n \in \mathbb{Z}$  specific to each  $n$  where  $b[n] \equiv \vec{d}_{N-1,n}^T \vec{x}_n^s$  and  $\epsilon$  is the bounding error term.*

Polynomial solutions of SDA problem and performance of Lenstra, Lenstra Jr., and Lovasz (LLL) algorithm for large number of inputs become highly prohibitive for  $N_p \gg 1$  [72]. Assume that  $\|x\|$  denotes the distance of the real number  $x$  to the closest integer, the maximum of  $\|\tilde{k}b[n]\|$  for  $n \in [0, N_p - 1]$  is smaller than some pre-defined  $\epsilon_p$  and there is some pre-defined bound  $M$  with  $M > \tilde{k}$ . LLL algorithm estimates  $\tilde{k}$  as  $\hat{k}$  satisfying  $1 < \hat{k} < 2^{N_p/2} M$  and the maximum of  $\|\hat{k}b[n]\|$  being smaller than  $\sqrt{5} \tilde{k} 2^{(N_p-1)/2} \epsilon_p$  with the number of operations depending on input size [72]. Error term for SDA is defined as  $\epsilon[n, \hat{k}] \equiv \|\hat{k}b[n]\|$  for  $n \in [0, N_p - 1]$ . Then,  $\bar{\epsilon}[\hat{k}] \equiv (1/N_p) \sum_{n=0}^{N_p-1} \epsilon[n, \hat{k}]$ ,  $\epsilon_{max}[\hat{k}] \equiv \max_n \{\epsilon[n, \hat{k}]\}$  and  $\epsilon_{min}[\hat{k}] \equiv \min_n \{\epsilon[n, \hat{k}]\}$  are indicators for observing how  $\hat{k}$  is close to the solution, i.e.,  $\tilde{k}$ .

Several candidate solution methods requiring more efforts to formally define and verify the solution algorithms are presented for Problems 1 and 2. Besides that, the set of the solutions which can be provided is constrained to the problems implementable with QPC setup without covering all the problems described in Problems 1 and 2. QPC period finding solution utilizes (21-24) in combination with a set of measurements at  $x = kT_s$ . QC algorithms exploit superposition generated with Hadamard transforms on two registers initially at  $|0\rangle|0\rangle$  and evolution with controlled unitary transforms  $U$  in BBs for a periodic function  $f(x) = f(x + r)$  [68]. QPC equation in (21) is utilized to find periodicity in  $f_n(\vec{x}) \equiv e^{i2\pi \vec{d}_{N-1,n}^T \vec{x}}$  for specific sets of  $\mathbf{X}_{N-1}$  and  $\vec{d}_{N-1,n}$ . The steps of QPC period finding algorithm are described as follows while the analogy to QC period finding is shown in Table 1:

- 0  $\vec{d}_{N-1,n}$  for  $n \in [0, N_p - 1]$ ,  $\mathbf{X}_{N-1}$  and  $\mathbf{X}_{N-1}^s$  are given initially where  $\mathbf{X}_{N-1}^s$  is defined in Problem 1. The function  $f_n(\vec{x}) = e^{i2\pi \vec{d}_{N-1,n}^T \vec{x}}$  has periodicity for  $\vec{x}$  with respect to the unknown period  $\tilde{k}$  and the given basis sets  $S_a : \{\vec{r}_a = \sum_{n=0}^{N_p-1} a_n \vec{x}_n^s, a_n \in \mathbb{Z}, n \in [0, N_p - 1]\}$  as follows:  $f_n(\vec{x}) = f_n(\vec{x} + \tilde{k} \vec{r}_a)$  while the target is to find  $\tilde{k}$ .
- 1 The wave function  $|\Psi_0\rangle$  of coherent source as a Gaussian packet is set up.
- 2 The superposition is due to QPC setup combining  $N_p$  paths on the screen and  $|\Psi_0\rangle$  where the initial state is denoted by  $\sum_{n=0}^{N_p-1} |\vec{x}_n^s\rangle |\Psi_0\rangle$ .
- 3 BB is the QPC setup with specially designed parameters providing  $\vec{x}_n$  in the grid  $\mathbf{X}_{N-1}$  and the vectors  $\vec{d}_{N-1,n}$  while related parameters  $A_{N-1,n}$ ,  $B_{N-1,n}$ ,  $\Upsilon_{N,n}$ ,  $\mathbf{H}_{N-1,n}$ ,  $\vec{c}_{N-1,n}$ , and the setup parameters  $S_\beta$ ,  $\vec{L}$ ,  $m$ ,  $\sigma_0$  and  $T_s$  to be optimally designed for generating  $\vec{x}_n^s$  and the best estimate of  $\tilde{k}$  by using  $I_N^G[k] = |\sum_{n=0}^{N_p-1} \gamma_{f,n}(\vec{x}_n^s, k) f_n(k \vec{x}_n^s)|^2$ .

**Table 1** The analogy between QC and QPC period finding algorithms

QC Period Finding Algorithm [68]		QPC Period Finding Algorithm		
Steps	Procedure	# Ops.	Procedure	# Ops.
0	a. The function $f(x)$ b. $x$ is integer, producing single bit output c. Periodic for $0 < r < 2^L$ integer: $f(x) = f(x+r)$ d. BB performing $U x\rangle y\rangle =  x\rangle y \oplus f(x)\rangle$	0	a. $f_n(\vec{x}) = e^{i2\pi \vec{d}_{N-1,n}^T \vec{x}}$ where $\vec{x}$ and $\vec{d}_{N-1,n}$ are tuned by the setup. b. The basis periodicity sets defined as $S_a: \{\vec{r}_a = \sum_{n=0}^{N_p-1} a_n \vec{x}_n^s, a_n \in \mathbb{Z}, n \in [0, N_p-1]\}$ for $\vec{x}_n^s \in \mathbf{X}_{N-1}^s$ c. $f_n(\vec{x}) = f_n(\vec{x} + \vec{r}_a)$ for $\vec{r}_a \in S_a$ d. QPC setup or BB performing $f_n(k \vec{x}_n^s)$ given $\vec{x}_n^s$ and integer $k$	0
1	Initial state: $ 0\rangle 0\rangle$	0	$ \Psi_0\rangle$ : coherent Gaussian wave packet	0
2	Superposition: $\frac{1}{\sqrt{2^t}} \sum_0^{2^t-1}  x\rangle 0\rangle$	0	$N_p$ paths to reach the detector with $\vec{x}_n^s$ for $n \in [0, N_p-1]$ and $\sum_{n=0}^{N_p-1}  \vec{x}_n^s\rangle  \Psi_0\rangle$	0
3	Black box (BB) $U$ : $\frac{1}{\sqrt{2^t}} \sum_0^{2^t-1}  x\rangle f(x)\rangle$	1	BB params. $\mathbf{X}_{N-1}^s, S_\beta, \vec{L}, m$ and $\sigma_0$ : $\Psi_N(k T_s) = \sum_{n=0}^{N_p-1} \Psi_{n,N}(k T_s)$ $= \sum_{n=0}^{N_p-1} \gamma_{f,n}(\vec{x}_n^s, k) f_n(k \vec{x}_n^s)$	1
4 & 5	a. IQFT: $(1/\sqrt{r}) \sum_0^{r-1}  l/r\rangle  \widehat{f}(l)\rangle$ b. Measure first register: $l/r$	$O(L^2)$	a. Measure $ \Psi_N(k T_s) ^2$ at various $k$ b. $IFFT_M$ at $p$ with $M \geq \tilde{k}$ : $\sum_{h=0}^{\tilde{k}-1} \Gamma_M^G[p/M, h/\tilde{k}]$	$O(M \log M)$
6	Continued fractions: $r$	$O(L^3)$	Check IFFT at $p \in [0, M-1]$ values for $M \geq \tilde{k}$ providing an estimation for $h/\tilde{k}$ for $h \in [0, \tilde{k}-1]$ and resulting in a converging estimation of $\tilde{k}$	Polynomial target

4-5 A set of  $M \geq \tilde{k}$  samples are taken on detector plane and IFFT operation with complexity  $O(M \log M)$  with the output time index  $p$  gives information about  $p/\tilde{k}$  and  $h/\tilde{k}$  for  $h \in [0, \tilde{k}-1]$  where  $\Gamma_M^G[p/M, h/\tilde{k}]$  in (28).

6 The number of samples at varying  $p$  values is increased for a converging and unbiased estimation of  $\tilde{k}$ . The problem is set as a parameter estimation problem for the set of damped sinusoids [73]. Traditional period finding algorithms are utilized to best estimate  $\tilde{k}$ , e.g.,  $O(M \log M)$  complexity or polynomial complexity for FFT based solutions in frequency estimation of damped sinusoidal signals.

Next, three approaches are introduced for the final three steps of the algorithm, i.e., Steps 4, 5 and 6. The first approach converts IFFT output to extract information about  $h/\tilde{k}$  by using the IFFT samples at  $p \in [0, M-1]$  in analogy to period finding method for conventional QC [68] as described in Table 1. The second approach checks the periodicity in the local maximum of  $I_N^G[k]$  and the third approach models the problem as a fundamental frequency estimation for a sum of sinusoidal signals.

### 8.1 Conversion of IFFT Output

IFFT operation with the number of samples  $M$  described in Steps 4&5 is simplified by using (21). Define discrete functions of  $n$  as  $g_1[n] \equiv e^{\vec{d}_{N-1,n}^T \vec{x}_n T_s}$ ,  $g_2[n] \equiv \vec{d}_{N-1,n}^T \vec{x}_n T_s$ ,  $g_3[n] \equiv \Upsilon_{N,n} e^{\vec{x}_n^T \mathbf{H}_{N-1,n} \vec{x}_n}$  and  $g_4[n]$  defined as  $e^{(A_{N-1,n} + i B_{N-1,n}) T_s^2}$ . Since  $\vec{d}_{N-1,n}$  and  $(2\pi)^{-1} T_s \vec{x}_n$  form an integer lattice for  $n \in [0, N_p - 1]$  with integer period  $\tilde{k}$ , the expression  $e^{i \vec{d}_{N-1,n}^T \vec{x}_n k T_s} = e^{i g_2[n] k}$  is converted to  $e^{i \tilde{G}_2[n] 2\pi k / \tilde{k}}$  due to periodicity with  $\tilde{k}$  where  $\tilde{G}_2[n]$  is a function mapping the interval  $[0, N_p - 1]$  into an integer between  $[0, \tilde{k} - 1]$  while depending on the relation between  $\vec{d}_{N-1,n}$  and  $\mathbf{X}_{N-1}^s$ . Then, IFFT output with size  $M$  denoted by  $IFFT_M\{I_N^G\}[p]$  becomes as follows:

$$\begin{aligned} &= \frac{1}{\sqrt{M}} \sum_{k=0}^{M-1} \sum_{n,l=0}^{N_p-1} g_{3,*}[n,l] g_{1,*}^k[n,l] g_{4,*}^{k^2}[n,l] e^{-\frac{i 2\pi k \Delta G_2[n,l]}{k}} e^{\frac{i 2\pi k p}{M}} \\ &= \sum_{n,l=0}^{N_p-1} g_{3,*}[n,l] \frac{1}{\sqrt{M}} \sum_{k=0}^{M-1} g_{1,*}^k[n,l] g_{4,*}^{k^2}[n,l] e^{-\frac{i 2\pi k \Delta G_2[n,l]}{k}} e^{\frac{i 2\pi k p}{M}} \end{aligned} \quad (26)$$

where  $g_{1,*}[n,l] \equiv g_1[n] g_1[l]$ ,  $g_{3,*}[n,l] \equiv g_3[n] g_3^*[l]$ ,  $g_{4,*}[n,l] \equiv g_4[n] g_4^*[l]$ , the set of coefficients of  $\omega_0 \equiv 2\pi / \tilde{k}$  is  $\Delta G_2[n,l] \equiv \tilde{G}_2[l] - \tilde{G}_2[n]$ . Dividing the set of  $[n,l]$  pairs in  $[0, N_p - 1] \times [0, N_p - 1]$  into  $\tilde{k}$  regions with index  $h \in [0, \tilde{k} - 1]$  denoted by  $R_h$  results in the following equality since  $\text{mod}(\Delta G_2[n,l], \tilde{k}) = h$ :

$$\begin{aligned} IFFT_M\{I_N^G\}[p] &= \sum_{h=0}^{\tilde{k}-1} \Gamma_M^G\left[\frac{p}{M}, \frac{h}{\tilde{k}}\right] \\ &= \sum_{h=0}^{\tilde{k}-1} \sum_{n,l \in R_h} g_{3,*}[n,l] \Omega_{n,l}^F\left(\frac{p}{M} - \frac{h}{\tilde{k}}\right) \end{aligned} \quad (27)$$

where  $\Gamma_M^G[p/M, h/\tilde{k}]$  is defined as follows:

$$\Gamma_M^G\left[\frac{p}{M}, \frac{h}{\tilde{k}}\right] = \sum_{n,l \in R_h} \frac{g_{3,*}[n,l]}{\sqrt{M}} \sum_{k=0}^{M-1} g_{1,*}^k[n,l] g_{4,*}^{k^2}[n,l] e^{i 2\pi k \left(\frac{p}{M} - \frac{h}{\tilde{k}}\right)} \quad (28)$$

and  $\Omega_{n,l}^F(x)$  is closely related to the discrete approximation of the continuous inverse Fourier transform of  $g_{1,*}^k[n,l] g_{4,*}^{k^2}[n,l]$  with respect to  $k$  by allowing the result at fractional values of the positions defined as follows:

$$\Omega_{n,l}^F(x) \equiv \frac{1}{\sqrt{M}} \sum_{k=0}^{M-1} g_{1,*}^k[n,l] g_{4,*}^{k^2}[n,l] e^{i 2\pi k x} \quad (29)$$

The structure of the IFFT output is best understood for finding the period of  $f(\vec{x}) = e^{i 2\pi \vec{d}_{N-1}^T \vec{x}}$  with path independent periodic function obtained with

uniform slit widths for each plane. This problem is classically tractable and numerically analyzed in Section 10 as a proof of concept. Assume that the intensity is normalized with  $\tilde{I}_N[k] \equiv \tilde{I}[k] \equiv e^{-2A_{N-1}k^2T_s^2} I_N[k]$  (obtained from  $I_N[k] \equiv I_N(kT_s)$ ) which results in the omission of the term  $g_{1,*}^{k^2}[n, l]$  in (26). Then, the equality in (26) is modified as follows by using the power series summation:

$$\begin{aligned}
IFFT_M\{\tilde{I}\}[p] &= \sum_{k=0}^{M-1} \sum_{n,l=0}^{N_p-1} \frac{g_{3,*}[n, l]}{\sqrt{M}} g_{1,*}^k[n, l] e^{-\frac{i2\pi k \Delta G_2[n, l]}{k}} e^{\frac{i2\pi k p}{M}} \\
&= \sum_{n,l=0}^{N_p-1} \frac{g_{3,*}[n, l]}{\sqrt{M}} \sum_{k=0}^{M-1} g_{1,*}^k[n, l] e^{-\frac{i2\pi k \Delta G_2[n, l]}{k}} e^{\frac{i2\pi k p}{M}} \\
&= \sum_{n=0}^{N_p-1} \sum_{l=0}^{N_p-1} \frac{g_{3,*}[n, l]}{\sqrt{M}} \frac{1 - \gamma_{n,l,p}^M}{1 - \gamma_{n,l,p}} \\
&= \sum_{h=0}^{\tilde{k}-1} \Gamma_M\left[\frac{p}{M}, \frac{h}{\tilde{k}}\right]
\end{aligned} \tag{30}$$

where  $\gamma_{n,l,p} \equiv g_{1,*}[n, l] e^{-\frac{i2\pi}{M\tilde{k}}(\Delta G_2[n, l]M - p\tilde{k})}$ . After dividing the  $(n, l)$  region with  $R_h$ ,  $\Gamma_M[p/M, h/\tilde{k}]$  is calculated as follows:

$$\Gamma_M\left[\frac{p}{M}, \frac{h}{\tilde{k}}\right] = \sum_{n,l \in R_h} \frac{g_{3,*}[n, l]}{\sqrt{M}} \frac{1 - g_{1,*}^M[n, l] e^{-i2\pi \frac{hM}{\tilde{k}}}}{1 - g_{1,*}[n, l] e^{i2\pi(\frac{p}{M} - \frac{h}{\tilde{k}})}} \tag{31}$$

If  $M = \tilde{k}$ , the rational term is  $(1 - g_{1,*}^{\tilde{k}}[n, l]) (1 - g_{1,*}[n, l] e^{i2\pi(p-h)/\tilde{k}})^{-1}$ . Similar to the Bertocco algorithm for the single sinusoid case [73], it is observed that exponentially increasing term  $(1 - g_{1,*}^M[n, l] e^{-i2\pi hM/\tilde{k}})$  in the numerator results in fast oscillations of the phase for each  $h \in [0, \tilde{k} - 1]$  if  $M < \tilde{k}$ . A function denoted by  $R[M]$  is introduced to utilize in the estimations as follows:

$$R[M] \equiv \frac{|IFFT_M\{\tilde{I}\}[0]|}{\frac{1}{M-1} \sum_{k=1}^{M-1} |IFFT_M\{\tilde{I}\}[k]|} \tag{32}$$

while it is expected to be maximized around  $M \approx \tilde{k}$ . High frequency components are averaged and their mean is compared with zero frequency component. Then, checking the samples of  $R[M]$  with respect to  $M$ , i.e., minimizing high frequency components, allows roughly determining  $\tilde{k}$ . The same periodicity is expected in  $R[M]$  since fluctuations are decreased at multiples of  $\tilde{k}$ .

## 8.2 Periodicity Detection in Local Maximum of Intensity

Periodicity  $\tilde{k}$  is heuristically found by checking local maximums in the measurement intensity  $\tilde{I}[k]$  satisfying the following theorem:

**Theorem 1** Assume that the set of real vectors  $\vec{c}_{N-1}$  and  $\vec{d}_{N-1}$ , and a non-uniform grid  $\mathbf{X}_{N-1}^s$  satisfy the following with the tuned physical setup giving the measurement in (21) and the normalized intensity  $\tilde{I}[k]$ :

1.  $\vec{d}_{N-1}$  and  $\mathbf{X}_{N-1}^s$  form an integer lattice with  $e^{i g_2[n] k} = e^{i \vec{d}_{N-1}^T \vec{x}_n T_s k}$  to be represented by  $e^{i \tilde{G}_2[n] 2\pi k / \tilde{k}}$ .
2.  $|H[k, \tilde{G}_2]| < |H[k, 0]|$  and  $|H[k_1, 0]| > |H[k_2, 0]|$  where  $0 < k < \tilde{k}$ ,  $k_2 < k_1 \leq \tilde{k}$ , and  $k, k_1, k_2 \in \mathbb{Z}$ , and  $H[k, \text{func}]$  is defined as follows:

$$\sum_{n=0}^{N_p-1} g_3[n] (g_1[n])^k e^{\frac{i 2\pi \text{func}[n] k}{\tilde{k}}} \quad (33)$$

where  $\text{func}[n] \in [0, \tilde{k} - 1]$  refers to a specific mapping of  $n \in [0, N_p - 1]$  with a discrete function  $\text{func}[\cdot]$  and  $H[k, 0]$  refers to the case where  $\text{func}[n] = 0$ . Then,  $\tilde{I}[\tilde{k}] > \tilde{I}[k]$  is satisfied for  $k \in [0, \tilde{k} - 1]$ .

The proof is provided in Appendix C. Checking local maximum  $\hat{k}$  with random samples of  $\vec{d}_{N-1}^T \vec{x}_n \hat{k} T_s / (2\pi)$  to verify for integer values determines the periodicity  $\tilde{k}$ . The extension of Theorem 1 for  $I_N^G[k]$  is required for the important and computationally hard problem of  $b[n] = \vec{d}_{N-1, n}^T \vec{x}_n^s$  compared with the classically efficient solutions for the case of  $b[n] = \vec{d}_{N-1}^T \vec{x}_n^s$ . The methods for frequency estimation of damped sinusoids as described in [73] is presented next.

### 8.3 Frequency Estimation for Sinusoidal Signals

The problem is considered as finding the fundamental frequency  $\omega_0 = 2\pi / \tilde{k}$  for the sum of complex sinusoidal signals [73] if (26) is transformed as follows:

$$I_N^G[k] = \sum_{n=0}^{N_p-1} \sum_{l=0}^{N_p-1} g_{3,*}[n, l] g_{1,*}^k[n, l] g_{4,*}^{k^2}[n, l] e^{-i \Delta G_2[n, l] \omega_0 k} \quad (34)$$

We drop the subscript  $N$  in the following and denote the samples of the intensity obtained with a setup composed of non-uniform slit widths as  $I^G[k]$  and as  $I[k]$  with uniform slit widths for each plane in the constrained case. Then, the effect of the additive white Gaussian noise (AWGN) is modeled as  $I_n^G[k] = I^G[k] + n[k]$  where  $n[k]$  is the receiver noise modeled as a Gaussian random process with independent samples. If Poisson distribution is assumed, then the noise has variance  $\sigma_k^2$  proportional to  $I^G[k]$ . Let us assume that  $I[k]$  in the second setup with constrained slit widths is normalized as  $\tilde{I}[k] = e^{-2 A_{N-1} (k T_s)^2} I[k]$  to exclude the effect of the constant multiplier  $A_{N-1}$  which is the same for each path. If the AWGN output intensity is normalized, then the noise is also amplified with  $\tilde{I}_n[k] = \tilde{I}[k] + \tilde{n}[k]$  where  $\tilde{n}[k] = e^{-2 A_{N-1} (k T_s)^2} n[k]$  with the variance  $\tilde{\sigma}^2[k] \equiv e^{-4 A_{N-1} (k T_s)^2} \sigma_k^2$ . In the

following discussion and Appendix D, it is assumed that  $I^*[k]$  and  $n^*[k]$  refer to  $I^G[k]$  and  $n[k]$ , respectively, for the general setup while referring to the normalized intensity  $\tilde{I}[k]$  and the noise  $\tilde{n}[k]$ , respectively, for the constrained setup. Similarly,  $\sigma^*[k]$  denotes  $\sigma_k$  for the general setup while denoting  $\tilde{\sigma}[k]$  for the constrained setup. Cramer-Rao lower bound for the estimate of  $\tilde{k}$  is provided in the following theorem while the proof is provided in Appendix D:

**Theorem 2** *Cramer-Rao lower bound for period finding in reciprocal integer lattice of QPC setup by using a set of intensity measurements in  $M$  different positions with sample points  $k_p T_s$  for  $p \in [0, M - 1]$  is given as follows:*

$$CRB(\tilde{k}) = \left(1 + \frac{\delta b(\hat{k})}{\delta \tilde{k}}\right)^2 / \sum_{p=0}^{M-1} \left(\frac{1}{\sigma^*[p]} \frac{\delta I^*[k_p]}{\delta \tilde{k}}\right)^2 \quad (35)$$

where  $b(\hat{k}) \equiv E\{\hat{k}\} - \tilde{k}$  is the bias while noise has zero mean.

Open issues in QPC based period finding and SDA solution are described next.

#### 8.4 Open Issues in Period Finding and SDA Solution

The proposed period finding methods for the Steps 4, 5 and 6 in Table 1 are heuristic. An open issue is to best utilize (27) with samples  $p \in [0, M - 1]$  by performing polynomial time complexity operations to estimate  $\tilde{k}$  in analogy to IFFT and continued fractions operations in conventional QC period finding algorithm with quantum gates [68]. Formal mathematical proof for determining the group of SDA problems with QPC solution and an exact algorithm finding the solution in Step-6 in Table 1 are open issues. It requires to analyze the relation among  $A_{N-1,n}$ ,  $B_{N-1,n}$ ,  $\Upsilon_{N,n}$ ,  $\mathbf{X}_{N-1}$ ,  $\mathbf{H}_{N-1,n}$ ,  $\vec{c}_{N-1,n}$  and  $\vec{d}_{N-1,n}$  in (21). SDA problem solution for a general set of  $b[n]$  is NP-hard [72]; however, the proposed  $b[n]$  is represented with  $\vec{d}_{N-1,n}^T \vec{x}_n^s$  as a specific instance limiting the space of the candidate SDA problems with potential solutions. Furthermore, it is an open issue whether the specific group of SDA problems which can be solved with QPC in an efficient manner can also be efficiently solved with classical computers with polynomial complexity of resources.

The extension of Theorem 1 for  $I_N^G[k]$  is an open issue which provides detection of periodicity by directly checking the periodicity in intensity. In addition, the existence of  $\tilde{k} \leq K_{pre} \equiv M$  for the proposed simple SDA problem (with  $b[n] \equiv \vec{d}_{N-1}^T \vec{x}_n^s$  and  $\tilde{I}[k]$ ) is heuristically checked by the existence of fluctuations. If there is no fluctuation, it is assumed as the absence of the bounded error  $\epsilon$  such that the solution does not exist for  $k \leq M$ . If there is a fluctuation, the set of fluctuating points are the candidates for a solution to be checked. Furthermore, practical algorithms of fundamental frequency estimation for the sums of sinusoidal signals should be developed for QPC [73]. Next, effects of non-classical paths discussed in [16, 17] are analyzed.



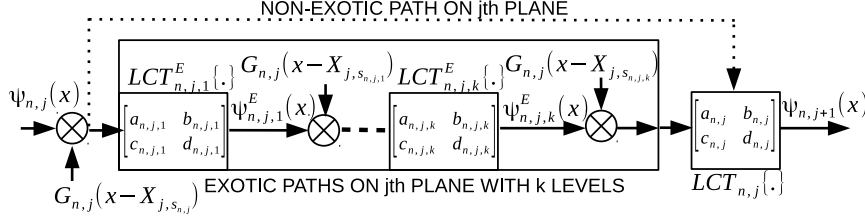


**Fig. 3** The representation of evolution of wave function  $\Psi_{n,j}(x)$  on  $j$ th plane in  $n$ th path as consecutive operations of non-classical movements  $LCT_{n,i}^E\{\cdot\}$  followed by multiplication of  $G_{n,j}(x - X_{j,s_{n,j,i}})$  for  $i \in [1, k]$  and finally after  $LCT_{n,j}\{\cdot\}$  resulting in  $\Psi_{n,j+1}(x)$ .

## 9 Effects of Exotic Paths

Evolved wave function is calculated by summing contributions from both *non-exotic* (or classical denoting the paths not including non-classical trajectories defined in [16, 17]) and non-classical paths (trajectories including movements on a single plane) by providing a complete formulation of QPC setup. A sample non-classical path is shown in Fig. 1(c) by forming a loop between the slits. Assume that the particle of  $n$ th path on  $j$ th plane makes  $k$  consecutive visits to slits in addition to the first slit with the index  $s_{n,j}$  and position  $X_{j,s_{n,j}}$  while the case with  $k = 0$  corresponds to the non-exotic path as shown in Fig. 3. The wave function in the non-classical path after  $k$ th slit denoted by  $\Psi_{n,j,k}^E(x)$  is explicitly provided in Appendix E for  $k$  bounded by  $N_E$ .  $LCT_{n,j,k}^E\{\cdot\}$  depends on the distance between the slits on  $j$ th plane defined as  $\Delta_x^E(j, k) \equiv |X_{j,s_{n,j,k}} - X_{j,s_{n,j,k-1}}|$  where  $X_{j,s_{n,j,k}}$  denotes the central position of  $k$ th visited slit and  $k = 0$  case corresponds to the position of the first slit on  $j$ th plane, i.e.,  $X_{j,s_{n,j,0}} \equiv X_{j,s_{n,j}}$ . Then, setting  $N_E$  and finding all paths for  $k \in [0, N_E]$  allow to include the effects of all possible non-classical paths.

Operator formalism for calculating Gouy phase in [16] is utilized to calculate time durations for the path distance  $\Delta_x^E(j, k)$  with  $t_{k-1,k}^E(j)$  defined as  $\Delta_x^E(j, k) / \Delta_v^E(j) = m \Delta_x^E(j, k) / \Delta_p^E(j)$  where  $\Delta_p^E(j) = \sqrt{\langle p^2 \rangle - \langle p \rangle^2}$  and  $\langle p^a \rangle$  for  $a \in [1, 2]$  is defined as  $\langle p^a \rangle \equiv \int_{-\infty}^{\infty} \Psi_j^*(x) ((\hbar / i) \delta / \delta x)^a \Psi_j(x) dx$ . Total number of different paths between  $j$ th and  $(j + 1)$ th planes including non-classical movements is denoted by  $N_{e,j} = S_{j,T} \sum_{k=0}^{N_E} (S_{j,T} - 1)^k$  while total number of all paths on  $i$ th plane for  $i \in [2, N]$  is given by  $N_{p,i}^E \equiv \prod_{j=1}^{i-1} N_{e,j}$ . Total number of paths on sensor plane is denoted by  $N_{p,N}^E$  much larger compared with the case including only non-exotic paths, i.e.,  $N_p$ . Total number of contributions and effects of the non-classical paths are simulated in Section 10. The first term  $S_{j,T}$  shows different selections of the first slit while the remaining  $k$  different slit movements occur in  $(S_{j,T} - 1)^k$  permutations. Finally, summing the contributions for different  $k$  values until  $N_E$  results in  $N_{e,j}$ .

**Table 2** QPC problems and simulation setup parameters

ID	Property	Value
<i>Sim</i> <sub>1</sub>	$N, S_1, S_2$	3, 2, 2
	$\sigma_0$ (nm)	500
	$\vec{X}_1^T$ (nm), $\vec{X}_2^T$ (nm)	$[-6031.9 \quad -2960.6 \quad 110.7 \quad 3181.9 \quad 6253.2]$ , $[-643.9 \quad -327.6 \quad -11.4 \quad 304.8 \quad 621.1]$
	$\vec{d}^T$ (m <sup>-2</sup> )	$[-11825366721.5 \quad -114848915118.2]$
	$\vec{L}^T$ (m), $\vec{\beta}^T$ (nm), $T_s$ ( $\mu$ m)	$[1 \quad 400 \times 10^{-6} \quad 1]$ , $[196.5 \quad 63.2]$ , 1
<i>Sim</i> <sub>2</sub>	$N, S_{1,T}, S_{2,T}, S_{3,T}$	4, 33, 198, 238
	$\sigma_0$ (nm)	65
	$\vec{L}^T$ (m), $\vec{\beta}^T$ (nm), $T_s$ (nm)	$[0.125 \quad 1 \quad 1 \quad 1]$ , $[125 \quad 175 \quad 225]$ , 37.69

**Table 3** Physical parameters

Symbol	Value
$m$ (kg)	$9.11 \cdot 10^{-31}$
$v_z$ (m/s)	$1.46 \cdot 10^7$
$\hbar$ (J $\times$ s)	$1.05 \cdot 10^{-34}$

**Table 4** Path counts on planes for *Sim*<sub>1</sub>

Type	Plane-2	Sensor
Non-exotic	5	25
$N_E = 1$	25	625
$N_E = 2$	105	11025
$N_E = 3$	425	180625

## 10 Numerical Simulations

Two different experiments are denoted by *Sim*<sub>1</sub> and *Sim*<sub>2</sub> performed for a simple SDA problem and energy-complexity trade off, respectively, as shown in Table 2. Main system parameters are shown in Table 3 with electron based setup verified for Gouy phase calculations in [16]. In *Sim*<sub>1</sub> and *Sim*<sub>2</sub>, it is assumed that the slit widths are constrained to be the same on each plane. Therefore,  $\tilde{I}[k]$ , i.e.,  $e^{-2A_{N-1}(kT_s)^2} I[k]$ , denotes the normalized intensity in the simulations as discussed in Section 8.3. Similarly,  $R[M]$  in (32) is defined with  $\tilde{I}[k]$ . In *Sim*<sub>2</sub>, a highly complex interference setup is realized. The difference between two neighbor slit positions on  $j$ th plane is chosen as  $(9.5 + u) \times \beta_j$  where  $u$  is a uniform random variable such that Gaussian slit approximation is satisfied with high accuracy.  $\beta_j$  is increased incrementally in the set  $\{125, 175, 225\}$  (nm) to reduce computational complexity for finding the desired intensity distributions with such a large number of paths.

### 10.1 Simulation-1: Period Finding and SDA Solution

A simple numerical SDA problem is realized by choosing  $b[n] \equiv \vec{d}^T \vec{x}_n^s$  where the vector  $\vec{d}$  being the same for each path makes the solution classically tractable. In other words, a classically solvable and simple problem is proposed to observe the period finding capability of QPC. In fact, the period of  $e^{i2\pi \vec{d}^T \vec{x}_n^s k}$  can be found classically in an efficient manner by computing

the summation  $\sum_{x_1^s} \dots \sum_{x_{N-1}^s} e^{i2\pi \vec{d}^T \vec{x}_n^s k}$  classically. The summation is calculated by separating the terms for each  $x_j^s$  where  $j \in [1, N-1]$  and then multiplying the results at the sampling point  $k$ . However, for the general case of  $n$ th path dependent  $\vec{d}_{N-1,n}$ , it becomes not possible to separate the summations while requiring to exploit the advantages of QPC summation. The simulation and analysis for more difficult SDA problems are open issues.

Total number of non-exotic paths is  $N_p = 25$  while the number of all paths including non-classical ones, i.e.,  $N_{p,N}^E$ , for varying  $N_E$  is shown in Table 4. As  $N_E$  increases,  $N_{p,N}^E$  becomes significantly large making it difficult to calculate the intensity. The intensity roughly converges as  $N_E$  increases to three.

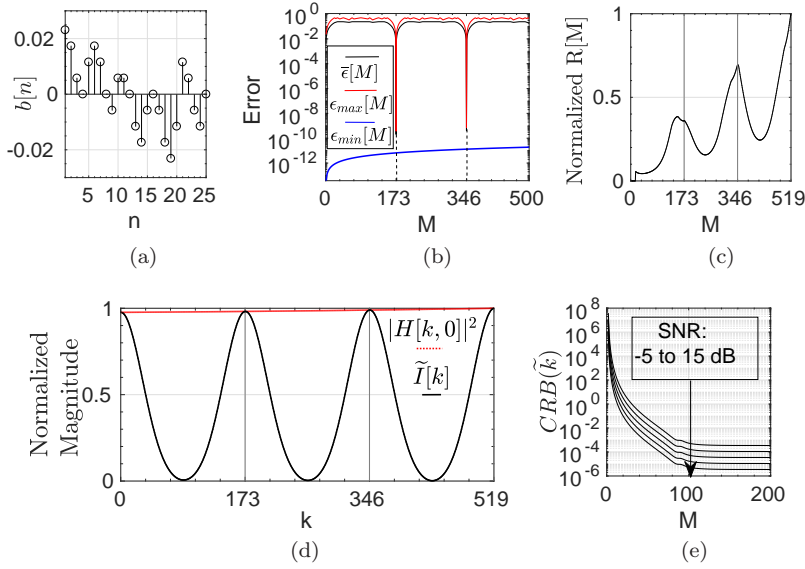


**Fig. 4** (a)  $b[n]$  for  $n \in [0, N_p - 1]$  defining SDA problem of  $Sim_1$ , (b) error terms in SDA problem including the minimum ones for varying  $M$ , (c)  $R[M]$  for varying  $M$  with similar periodicity, (d) normalized  $\tilde{I}[k]$  and  $|H[k, 0]|^2$  for varying  $k$ , and (e) Cramer-Rao bound for varying number of samples in  $[0, M - 1]$  and SNR in  $[-5, 0, 5, 10, 15]$  dB.

The fractional numbers forming the SDA problem are shown in Fig. 4(a). They are chosen to satisfy  $\tilde{k} = 173$ . In Fig. 4(b), error terms  $\bar{\epsilon}[M]$ ,  $\epsilon_{max}[M]$  and  $\epsilon_{min}[M]$  are shown for  $Sim_1$ . The mean error is smaller than  $10^{-8}$  for  $M = \tilde{k} = 173$ , assumed to be the SDA solution with accuracy of eight digits.

In Fig. 4(d), normalized  $\tilde{I}[k]$  and  $|H[k, 0]|^2$  are shown satisfying the Theorem 1 such that satisfying  $\tilde{I}[\tilde{k}] > \tilde{I}[k]$  and  $\tilde{I}[k] < |H[k, 0]|^2$  for  $0 < k < \tilde{k}$  with increasing  $|H[k, 0]|$ . *IFFT* based method provides an accurate estimation of  $\tilde{k}$  as shown in Fig. 4(d). Fluctuations are more visible as  $M$  increases at multiples of 173 while the maximum points of  $R[M]$  show periodicity of 173 as shown in Fig. 4(c). CRB is shown for varying SNR defined as  $I^2[k_p] / \sigma_p^2$  in

Fig. 4(e) with a low bound for the number of samples larger than a few tens. Therefore, estimation methods for damped sinusoids can be applied such as the ones in [73].

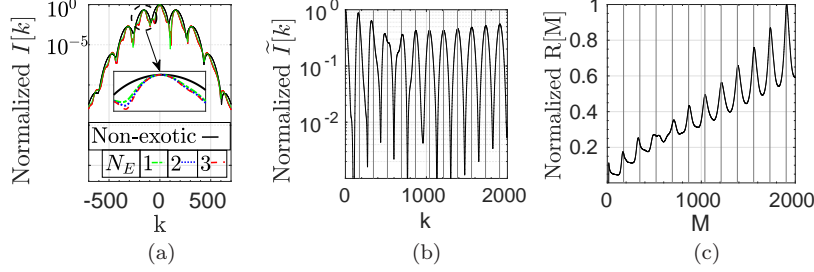


**Fig. 5** (a)  $I[k]$  (with the maximum normalized to unity) by including non-classical paths and for varying  $N_E$  where the middle part shows zoomed intensity distribution at the center, (b) normalized  $\tilde{I}[k]$  and (c)  $R[M]$  for varying  $k$  and  $M$ , respectively, with the same  $x$  axis and periodicity, for the case of  $N_E = 3$  where the lines show multiples of  $\tilde{k} = 173$ .

$I[k]$ , i.e.,  $e^{2A_{N-1}(kT_s)^2} \tilde{I}[k]$ , is normalized by setting the maximum value to unity as shown in Fig. 5(a) while including non-classical paths for varying  $N_E$ . The main structure of the distribution is preserved while effects for increasing  $N_E$  are attenuated as shown in Fig. 5(b) for the case of  $N_E = 3$  where normalized  $\tilde{I}[k]$  periodicity for varying  $k$  and the value of  $\tilde{k}$  are still reliably extracted. The same observation is preserved in normalized  $R[M]$  for varying  $M$  in Fig. 5(c). Utilizing values of  $\tilde{I}[k]$  for large  $k$  requires higher precision measurement instruments due to significant attenuation in  $I[k]$  at distant sample locations as shown in Fig. 5(a) and longer time to collect particles. Special tuning and design of QPC setup are required for efficient solutions exploiting QPC.

## 10.2 Simulation-2: Energy Flow and Complexity

Energy flow versus interference complexity trade off for  $Sim_2$  is shown in Figs. 6 and 7. In Fig. 6(a), the positions of the slits are shown where a larger number of slits are utilized in consecutive planes to cover the spread intensity distribution. In Fig. 6(b), complicated interference patterns are shown for the planes with the indices  $j \in [2, 4]$  while the Gaussian source ( $j = 0$ ) and the free space propagated version ( $j = 1$ ) are also shown. In Fig. 6(c), path amplitudes defined in (15) are shown for  $j \in [2, 4]$  while the number of paths is marked for  $\epsilon = 0.01$  for the definition of energy constrained Hilbert space in (16) modeled with  $D_j(\epsilon)$ . The regions of the slits on  $(j + 1)$ th plane where a slit on  $j$ th plane creates a path with high interference amplitude are shown in Figs. 6(d) and (e). Fig. 6(d) shows the left and right boundaries of the slit positions at  $x_{j+1}$  corresponding to each slit at  $x_j$  for  $j = 1$  and 2. The paths are shown in Fig. 6(e) by connecting the slits with a visual representation starting from the

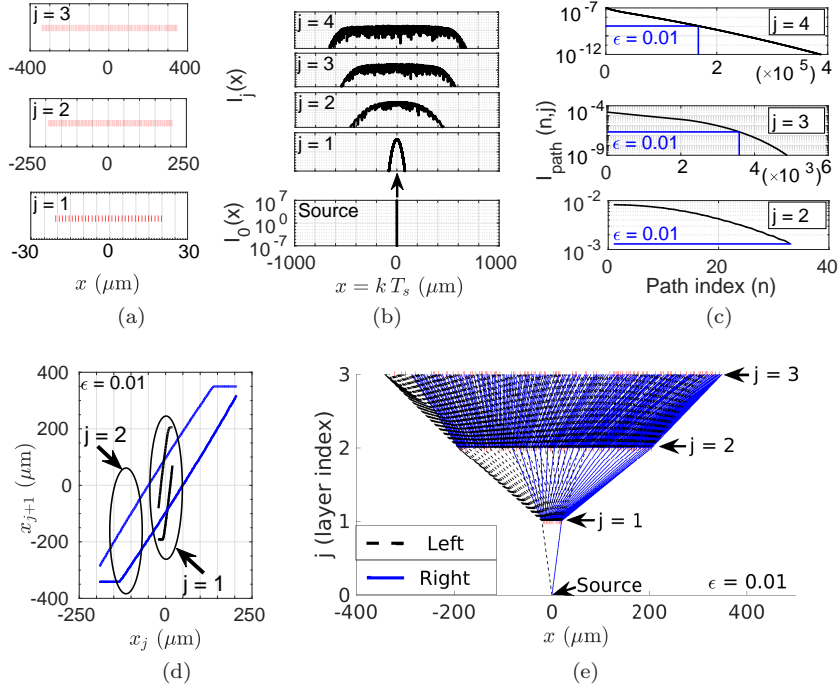


**Fig. 6** Energy-complexity trade off where (a) the slit positions for  $j \in [1, 3]$ , (b)  $I_j(x)$  for  $j \in [1, 4]$ , (c)  $I_{\text{path}}(n, j)$  on  $j$ th plane for  $j \in [2, 4]$ , (d) the slit positions on  $(j+1)$ th plane ( $x_{j+1}$ ) having a large amplitude path evolving from the slits on  $j$ th plane with the position  $x_j$ , (e) the same relation in (d) visually with the region of slits on  $(j+1)$ th plane marked with the left and right boundaries for the paths evolving from the slits on  $j$ th plane.

source until the slits of the third plane. The left and right boundaries form a region where the slits on consecutive planes form high amplitude paths. The leftmost slit on first plane at  $x = -20.63 \mu\text{m}$  forms high amplitude paths with the slits having the positions between  $(-191.2, -81.19) \mu\text{m}$  (marked as left and right boundaries) including  $\approx 57$  neighbor slits on the second plane.

Fig. 7 shows the results of energy-complexity trade off for varying  $\epsilon \in \{0, 0.01, 0.1, 0.5\}$ . Fig. 7(a) shows  $P_j$  versus  $D_j(\epsilon)$  for varying  $\epsilon$  and the plane index  $j$ .  $P_j$  drops to approximately  $5.88 \times 10^{-3}$  on the fourth plane while  $D_j(\epsilon)$  significantly increases to the values between  $1.34 \times 10^4$  and  $1.55 \times 10^6$  for  $\epsilon$  between 0 and 0.5. The performance parameter  $D_j(\epsilon) \times P_j$  is simulated in Fig. 7(b) showing a significantly increasing size of energy constrained Hilbert space with the number of planes while the exact calculation of intensity requires the calculation of all  $33 \times 198 \times 238 = 1555092$  paths. In Fig. 7(c), the negative volume of the Wigner distribution ( $V_N(j)$ ) is compared with the  $\log_2(\cdot)$  of the number of paths as a complexity performance metric assuming to be implemented with qubits. It is observed that increasing logarithmic complexity shows a parallel relation with the increasing negative volume of the Wigner function as another supporting observation of the non-classical resource struc-

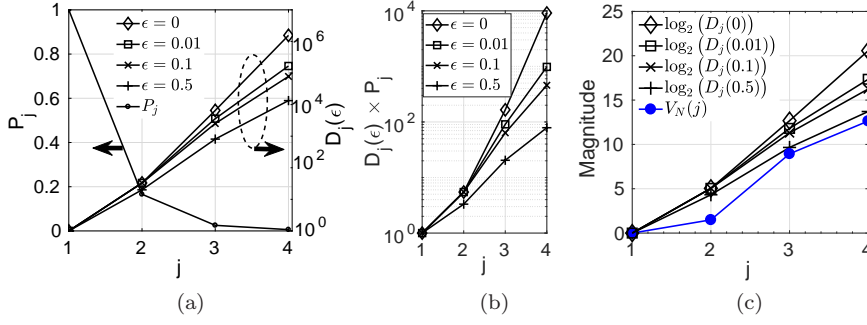


**Fig. 7** (a) The probability  $P_j$  versus the number of paths  $D_j(\epsilon)$ , (b)  $D_j(\epsilon) \times P_j$  and (c) the comparison of logarithmic number of paths with the negative volume of Wigner function ( $V_N(j)$ ) for the normalized wave function on each layer for  $j \in [1, 4]$  and for varying  $\epsilon \in \{0, 0.01, 0.1, 0.5\}$  showing a correlated increase in both of them.

ture of QPC. It requires further analysis for the parametric definition of the amount of resources. The positive and negative parts of the Wigner function for the wave functions on the second, third and fourth planes are shown in Figs. 8(a), (b) and (c), respectively. Wave functions are normalized on each plane to satisfy  $\int \int W(x, p) dx dp = 1$ . It is observed that as the layer index  $j$  increases, the number of highly interfering time-momentum locations increases with a spread in the area of the Wigner function.

In Fig. 9, the cumulative summations defined in (17) in Section 6 for the contributions of the sorted paths with respect to the three different types of path sorting methods are shown. The cumulative sums on the third and fourth planes are shown in Figs. 9(a) and (b), respectively, for the sampling positions of  $kT_s \in \{-20, 0, 20\} \mu\text{m}$ . Cumulative summation with Type-a is calculated by sorting the paths with respect to the descending probability of the particle to evolve through the specific path. Type-b is calculated by sorting the indices with respect to the descending magnitude of the intensity at the specific sampling location but not with respect to the total probability at all sampling locations. Finally, in Type-c, the paths in Type-b are coupled one by one in the order of descending magnitude to cancel each other. It is clearly observed that Type-b and Type-c having local characteristics tuned to the specific sampling point reach the stable cumulative intensity earlier compared with Type-a. If the paths are chosen to cancel each other in Type-c, then there is still oscillation and a nonlinear increase in the cumulative summation. It still requires a large number of paths to be summed to find the stable level of intensity on the sampling positions. Furthermore, there is not any apparent way to find the correct paths which approximately cancel each other among the exponentially increasing number of paths. Therefore, sorting and limiting the paths with respect to the probability with the complexity term  $\epsilon$  do not provide the required sets of the paths applicable at all sampling positions. In other words,  $D_j(\epsilon)$  at  $\epsilon = 0$  can be more reliable to cover all the sampling

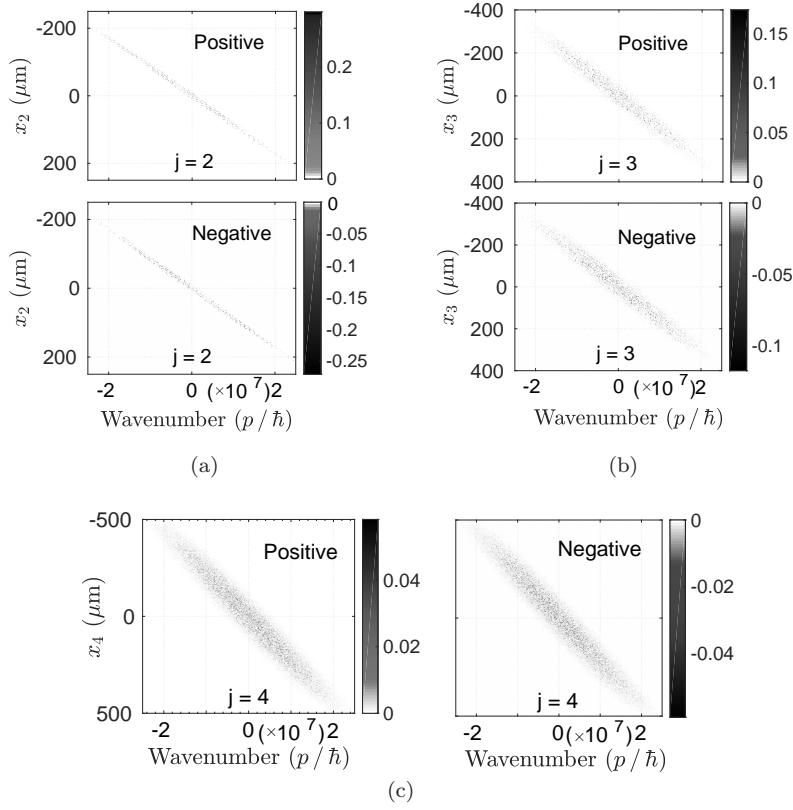


**Fig. 8** The positive and negative parts of the Wigner function for the wave functions on (a) the second, (b) the third, and (c) the fourth layers.

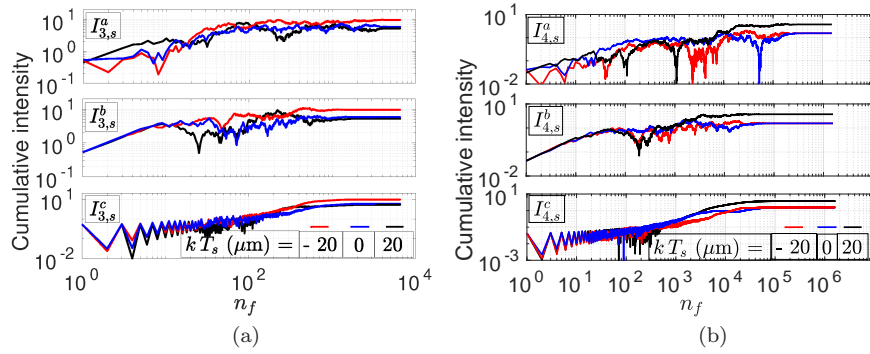


**Fig. 9** Cumulative summations defined in (17) in Section 6 for the contributions of the sorted paths with respect to the Type-a, b and c path sorting methods on the (a) third and (b) fourth planes.

locations. Therefore, QPC energy-complexity trade off provides a significantly large energy constrained Hilbert space.

## 11 Discussion and Open Issues

QPC system design requires further efforts listed as follows to be experimentally realized and improved for solutions of different numerical problems:

1. Modifying (14) with exponentially increasing number exotic paths.
2. Determining the complexity class of calculating QPC output intensity and comparing with universal classical or quantum computers.
3. Determining the set of period finding related problems which can be efficiently solved while in particular all the open issues regarding the utilization of QPC for SDA solutions described in Section 8.4.
4. The best utilization of (14) for computational purposes in addition to the practical problems presented.
5. Experimental verification and realization of Gaussian slits and mathematical modeling of QPC systems with non-Gaussian arbitrary slit properties.
6. Minimization of decoherence due to unintentional interactions with the particles during propagation [74].
7. Designing novel diffraction geometries in addition to the planar ones to solve different number theoretical problems as a universal system design based on history based resources.

## 12 Conclusion

A low hardware optical QC architecture is presented combining all-in-one targets: practical problem solving capability, energy efficient processing of sources, using only coherent or classical particle sources including both bosons and fermions, transforming the particle source through the simple classical optics and intensity measurement with simple particle detectors. The method denoted by QPC exploits MPD of the particles by creating exponentially increasing number of propagation paths through the slits in consecutive diffraction planes. Non-Gaussian nature of the propagating wave function is exploited for QC purposes with Feynman's path integral approach and numerical analysis is provided showing increasing negative volume of Wigner function. QPC promises solutions for two practical and hard number theoretical problems: partial sum of Riemann theta function and period finding for solving specific instances of Diophantine approximation problem. Open issues including the best utilization of QPC for computing purposes and modification of diffraction system for covering different problems are discussed.



**Table 5** Iteration parameters for FPI modeling

	Formula		Formula
$\Psi_0(x)$	$\exp(-x^2 / (2\sigma_0^2)) / \sqrt{\sigma_0 \sqrt{\pi}}$	$\vec{p}_1^T$	$[p_{1,1} \dots p_{1,N-1}]$
$A_0$	$-m^2 \sigma_0^2 / (2\hbar^2 t_{0,1}^2 + 2m^2 \sigma_0^4)$	$\vec{p}_2^T, \vec{p}_3^T$	$[p_{2,2} \dots p_{2,N-1} 0], [p_{3,2} \dots p_{3,N-1} 0]$
$B_0$	$\hbar m t_{0,1} / (2\hbar^2 t_{0,1}^2 + 2m^2 \sigma_0^4)$	$\chi_0$	$\pi^{-1/4} \sqrt{m \sigma_0 / (m \sigma_0^2 + \imath \hbar t_{0,1})}$
$A_1$	$\beta_1^2 m^2 (2A_0 \beta_1^2 - 1) / (2\zeta_1)$	$\chi_{1,n}$	$\sqrt{\xi_1} \exp(p_{1,1} X_{1,s_{n,1}}^2)$
$B_1$	$(2B_0 \beta_1^4 m^2 + \hbar m t_{1,2} \varrho_1) / (2\zeta_1)$	$C_{1,n}, D_{1,n}$	$\zeta_{1,c} X_{1,s_{n,1}}, \zeta_{1,d} X_{1,s_{n,1}}$
$j$	Symbol	Formula	
$[1, N-1]$	$p_{1,j}$	$-(2\hbar t_{j,j+1}(A_{j-1} + \imath B_{j-1}) + \imath m) / (2\imath \zeta_j)$	
	$\zeta_j, \xi_j$	$\beta_j^2 m + \hbar t_{j,j+1} (2\beta_j^2 (B_{j-1} - \imath A_{j-1}) + \imath), \beta_j^2 m / \zeta_j$	
	$\varrho_j$	$4\beta_j^4 (A_{j-1}^2 + B_{j-1}^2) - 4A_{j-1}\beta_j^2 + 1$	
	$\zeta_j$	$4B_{j-1}\beta_j^4 \hbar m t_{j,j+1} + \beta_j^4 m^2 + \hbar^2 t_{j,j+1}^2 \varrho_j$	
	$\zeta_{j,c}, \zeta_{j,d}$	$(2B_{j-1}\hbar m t_{j,j+1} \beta_j^2 + \beta_j^2 m^2) / \zeta_j, \hbar m t_{j,j+1} (2A_{j-1} \beta_j^2 - 1) / \zeta_j$	
$j$	Symbol	Formula	
$[2, N-1]$	$p_{2,j}, p_{3,j}$	$-\beta_j^2 \hbar t_{j,j+1} / (2\imath \zeta_j), -\hbar t_{j,j+1} / (\imath \zeta_j)$	
	$p_{4,j}, p_{5,j}$	$\beta_j^2 \zeta_{j,c}, -2\hbar t_{j,j+1} A_j / m$	
	$A_j, B_j$	$\beta_j^2 m^2 (2A_{j-1} \beta_j^2 - 1) / (2\zeta_j), (2B_{j-1} \beta_j^4 m^2 + \hbar m t_{j,j+1} \varrho_j) / (2\zeta_j)$	
	$C_{j,n}$	$\zeta_{j,c} X_{j,s_{n,j}} + p_{4,j} C_{j-1,n} + p_{5,j} D_{j-1,n}$	
	$D_{j,n}$	$\zeta_{j,d} X_{j,s_{n,j}} - p_{5,j} C_{j-1,n} + p_{4,j} D_{j-1,n}$	
	$\chi_{j,n}$	$\sqrt{\xi_j} \exp(p_{1,j} X_{j,s_{n,j}}^2) \times \exp(p_{2,j} (C_{j-1,n} + \imath D_{j-1,n})^2) \times \exp(p_{3,j} (C_{j-1,n} + \imath D_{j-1,n}) X_{j,s_{n,j}})$	

## A Iterative Formulation of Path Integrals

Throughout the appendices, various formulations are listed in Table 5. In the following, all the calculations are performed for the specific  $n$ th path assuming the corresponding slit width parameters are given by the values of  $\beta_j$  on  $j$ th plane for  $j \in [1, N-1]$ . Therefore, all the following parameters depend on the path index  $n$  without explicitly showing, e.g.,  $A_j$  and  $B_j$  should be replaced with  $A_{j,n}$  and  $B_{j,n}$ , respectively, for the specific  $n$ th path. The same is valid for the remaining parameters except the local parameters  $C_{j,n}$ ,  $D_{j,n}$  and  $\chi_{j,n}$ . They depend directly on the slit positions and accordingly on  $n$  such that they are denoted by including the path index  $n$  for  $j$ th plane as  $C_{j,n}$ ,  $D_{j,n}$  and  $\chi_{j,n}$ . Similarly,  $\vec{c}_{N-1}$  and  $\vec{d}_{N-1}$  should be replaced by  $\vec{c}_{N-1,n}$  and  $\vec{d}_{N-1,n}$ , respectively. The final resulting matrix  $\mathbf{H}$  utilized in (13) should be replaced with  $\mathbf{H}_{N-1,n}$  as in (14). Only the parameters  $A_0$ ,  $B_0$  and  $\chi_0$  are path independent. Therefore, the corresponding numerical results of the expressions for varying slit widths on each path are obtained by changing  $\beta_j$  on  $j$ th plane

for the corresponding path. After integration in (12), the following is obtained:

$$\Psi_{n,j}(x) = \chi_0 \left( \prod_{k=1}^{j-1} \chi_{k,n} \right) e^{(A_{j-1} + \iota B_{j-1})x^2 + (C_{j-1,n} + \iota D_{j-1,n})x} \quad (36)$$

where  $j \in [1, N]$ ,  $x$  corresponds to the position in  $x$ -axis on  $j$ th plane and iterative variables  $\chi_{j,n}$ ,  $A_j$ ,  $B_j$ ,  $C_{j,n}$  and  $D_{j,n}$  are defined in Table 5. The first integration is obtained with  $\Psi_0(x)$  by free propagation until the first slit plane resulting in  $A_0, B_0, \chi_0$  while  $C_0 = D_0 = 0$ . The second LCT results in  $A_1, B_1, C_{1,n}, D_{1,n}, \chi_{1,n}$  where  $p_{1,j}, \varsigma_j, \xi_j, \varrho_j, \zeta_j, \zeta_{j,c}$  and  $\zeta_{j,d}$  are defined for  $j \in [1, N-1]$ . Then, the iterations for  $A_j, B_j, C_{j,n}, D_{j,n}, \chi_{j,n}, p_{2,j}, p_{3,j}, p_{4,j}, p_{5,j}$  and  $\chi_{T,j} \equiv \chi_0 \prod_{k=1}^j \chi_{k,n}$  are obtained for  $j \in [2, N-1]$ . An iterative relation is obtained as follows:

$$\begin{bmatrix} C_{j,n} \\ D_{j,n} \end{bmatrix} = \begin{bmatrix} \zeta_{j,c} \\ \zeta_{j,d} \end{bmatrix} X_{j,s_{n,j}} + \begin{bmatrix} p_{4,j} & p_{5,j} \\ -p_{5,j} & p_{4,j} \end{bmatrix} \begin{bmatrix} C_{j-1,n} \\ D_{j-1,n} \end{bmatrix} \quad (37)$$

Performing iterations results in  $C_{N-1,n} = \vec{c}_{N-1}^T \vec{x}_{N-1,n}$  and  $D_{N-1,n} = \vec{d}_{N-1}^T \vec{x}_{N-1,n}$  where  $j$ th element of the vector  $\vec{x}_{N-1,n}$  of the length  $N-1$  is defined as  $X_{j,s_{n,j}}$ , and the row vectors  $\vec{c}_j^T$  and  $\vec{d}_j^T$  are defined as follows:

$$\begin{bmatrix} \vec{c}_j^T \\ \vec{d}_j^T \end{bmatrix} = [\vec{v}_{0,j} \ \vec{v}_{1,j} \ \dots \ \vec{v}_{j-1,j}] \quad (38)$$

where  $\vec{v}_{k,j}$  for  $k \in [0, j-1]$ , utilized to obtain  $C_{j,n} = \vec{c}_j^T \vec{x}_{j,n}$  and  $D_{j,n} = \vec{d}_j^T \vec{x}_{j,n}$ , is given as follows:

$$\vec{v}_{k,j} \equiv \left( \prod_{i=1}^{j-1-k} \begin{bmatrix} p_{4,j+1-i} & p_{5,j+1-i} \\ -p_{5,j+1-i} & p_{4,j+1-i} \end{bmatrix} \right) \begin{bmatrix} \zeta_{k+1,c} \\ \zeta_{k+1,d} \end{bmatrix} \quad (39)$$

and the matrix multiplication symbol  $\prod_{i=1}^k \mathbf{U}_i$  denotes  $\mathbf{U}_1 \mathbf{U}_2 \dots \mathbf{U}_k$  for any matrix  $\mathbf{U}_i$  for  $i \in [1, k]$ . The following is obtained after inserting the resulting expressions of  $C_{N-1,n}$  and  $D_{N-1,n}$  into  $\chi_{T,N-1}$ :

$$\begin{aligned} \chi_{T,N-1} &\equiv \chi_0 \left( \prod_{j=1}^{N-1} \sqrt{\xi_j} \right) e^{\vec{p}_1^T (\vec{x}_{N-1,n} \odot \vec{x}_{N-1,n})} \times e^{\vec{p}_2^T ((\mathbf{G} \vec{x}_{N-1,n}) \odot (\mathbf{G} \vec{x}_{N-1,n}))} \\ &\times e^{\vec{p}_3^T ((\mathbf{G} \vec{x}_{N-1,n}) \odot (\mathbf{E}_1 \vec{x}_{N-1,n}))} \end{aligned} \quad (40)$$

where  $\odot$  denotes the point-wise product,  $\mathbf{G}$  and  $\mathbf{E}_1$  are defined as follows:

$$\mathbf{G} \equiv \begin{bmatrix} \mathbf{E}_2 \mathbf{V}_L & \mathbf{0}_{N-2} \\ \mathbf{0}_{N-2}^T & \mathbf{0} \end{bmatrix}; \quad \mathbf{E}_1 \equiv \begin{bmatrix} \mathbf{0}_{N-2} & \mathbf{I}_{N-2} \\ \mathbf{0} & \mathbf{0}_{N-2}^T \end{bmatrix} \quad (41)$$

while  $\mathbf{E}_2$  has  $j$ th row as  $[\mathbf{0}_{2(j-1)}^T \ \mathbf{1} \ \mathbf{0}_{2(N-2-j)}^T]$ ,  $\mathbf{V}_L$  is the matrix whose  $j$ th column is given by  $[\mathbf{0}_{2(j-1)}^T \ \vec{v}_{j-1,j}^T \ \dots \ \vec{v}_{j-1,N-2}^T]^T$ ,  $\mathbf{0}_k$  is the column vector of zeros of length  $k$ , the sizes of  $\mathbf{E}_2$  and  $\mathbf{V}_L$  are  $(N-2) \times (2N-4)$  and  $(2N-4) \times (N-2)$ , respectively, and  $\mathbf{G}$  and  $\mathbf{E}_1$  are  $(N-1) \times (N-1)$ . Then, the resulting wave function  $\Psi_{n,N}(x)$  is given by the following:

$$\begin{aligned} \Psi_{n,N}(x) &= \Upsilon_N e^{\sum_{k=1}^3 \vec{p}_k^T \left( (\mathbf{M}_{1,k} \vec{x}_{N-1,n}) \odot (\mathbf{M}_{2,k} \vec{x}_{N-1,n}) \right)} \\ &\times e^{(A_{N-1} + \iota B_{N-1})x^2 + (\vec{c}_{N-1}^T + \iota \vec{d}_{N-1}^T) \vec{x}_{N-1,n} x} \end{aligned} \quad (42)$$

where  $\Upsilon_j = \chi_0 \left( \prod_{i=1}^{j-1} \sqrt{\xi_i} \right)$ ,  $\mathbf{M}_{1,1} = \mathbf{M}_{2,1} = \mathbf{I}_{N-1}$ ,  $\mathbf{M}_{1,2} = \mathbf{M}_{2,2} = \mathbf{G}$ ,  $\mathbf{M}_{1,3} = \mathbf{G}$ ,  $\mathbf{M}_{2,3} = \mathbf{E}_1$ ,  $\mathbf{I}_k$  is identity matrix of size  $k$ , complex valued column vectors  $\vec{p}_k$  for  $k \in [1, 3]$ , real valued iterative variables  $A_j$  and  $B_j$ , and complex valued iterative variable  $\xi_j$  are

defined in Table 5, and  $\vec{x}_{N-1,n} \equiv [X_{1,s_{n,1}} X_{2,s_{n,2}} \cdots X_{N-1,s_{n,N-1}}]^T$ . Intensity distribution on screen is  $I_N(x) = |\Psi_N(x)|^2$  which is equal to  $|\sum_{n=0}^{N_p-1} e^{(A_{N-1} + i B_{N-1}) x^2} \Upsilon_N e^{r\{\vec{x}_n\}} e^{\vec{c}^T \vec{x}_n} e^{i \vec{d}^T \vec{x}_n}|^2$  where  $I_j(x) = |\Psi_j(x)|^2$  denotes the intensity or the probability of detection on  $j$ th plane for  $j \in [0, N]$ ,  $I_0(x) \equiv |\Psi_0(x)|^2$ , the subscript  $N-1$  is dropped from the vectors to simplify the notation, e.g.,  $r\{\vec{x}_n\} \equiv \sum_{k=1}^3 \vec{p}_k^T ((\mathbf{M}_{1,k} \vec{x}_n) \odot (\mathbf{M}_{2,k} \vec{x}_n))$ ,  $\vec{x}_n \equiv \vec{x}_{N-1,n}$ ,  $\vec{c} \equiv \vec{c}_{N-1}$  and  $\vec{d} \equiv \vec{d}_{N-1}$ . It can be easily shown that  $r\{\vec{x}_n\}$  is equal to  $\vec{x}_n^T \mathbf{H} \vec{x}_n$  where the proof is in Appendix B and the matrix  $\mathbf{H}$  is given as  $\mathbf{H} = \sum_{k=1}^3 \mathbf{M}_{2,k}^T \text{diag}\{\vec{p}_k\} \mathbf{M}_{1,k}$  where  $\text{diag}\{\vec{y}\}$  is the operator creating a diagonal matrix with the elements composed of the vector  $\vec{y}$ .

## B Generation of the H-matrix

$\sum_{k=1}^3 \vec{p}_k^T ((\mathbf{M}_{1,k} \vec{x}_n) \odot (\mathbf{M}_{2,k} \vec{x}_n))$  is transformed to four different equalities. Firstly, it equals to  $\stackrel{1}{=} \sum_{k=1}^3 \text{Tr}\{\text{diag}\{\vec{p}_k\} \mathbf{M}_{1,k} \vec{x}_n \vec{x}_n^T \mathbf{M}_{2,k}^T\}$  where the equality is obtained by transforming the inner and point-wise product combination into a trace. Then,  $\stackrel{2}{=} \sum_{k=1}^3 \text{Tr}\{\mathbf{M}_{2,k}^T \text{diag}\{\vec{p}_k\} \mathbf{M}_{1,k} \vec{x}_n \vec{x}_n^T\}$  and  $\stackrel{3}{=} \text{Tr}\{(\sum_{k=1}^3 \mathbf{M}_{2,k}^T \text{diag}\{\vec{p}_k\} \mathbf{M}_{1,k}) \vec{x}_n \vec{x}_n^T\}$  are obtained due to the permutation and the addition properties of the trace, respectively. Finally,  $\stackrel{4}{=} \text{Tr}\{\vec{x}_n^T (\sum_{k=1}^3 \mathbf{M}_{2,k}^T \text{diag}\{\vec{p}_k\} \mathbf{M}_{1,k}) \vec{x}_n\}$  is obtained with the permutation property. Then, the quadratic form is obtained.

## C Proof of Theorem 1

The intensity at  $\tilde{k} - k$  for  $k \in [1, \tilde{k}]$  is given as follows due to the definition in (21) and the first condition in Theorem 1:

$$\tilde{I}[\tilde{k} - k] \stackrel{1}{=} \left| \sum_{n=0}^{N_p-1} g_3[n] (g_1[n])^{\tilde{k}-k} e^{-i 2 \pi \tilde{G}_2[n] k / \tilde{k}} \right|^2 = |H[\tilde{k} - k, \tilde{G}_2]|^2 \quad (43)$$

Then,  $\tilde{I}[\tilde{k} - k] \stackrel{2}{<} |\sum_{n=0}^{N_p-1} g_3[n] (g_1[n])^{\tilde{k}-k}|^2 \stackrel{3}{<} \tilde{I}[\tilde{k}] = |\sum_{n=0}^{N_p-1} g_3[n] (g_1[n])^{\tilde{k}}|^2$  are obtained with the second condition in Theorem 1.

## D Proof of Theorem 2

The conditional probability for the sample at  $k_p$  is given by the following:

$$p(I_n^*[k_p]|\tilde{k}) = (2\pi \tilde{\sigma}_p^2)^{-1/2} e^{-(I_n^*[k_p] - I^*[k_p])^2 / (2\tilde{\sigma}_p^2)} \quad (44)$$

where  $\tilde{\sigma}_p \equiv \sigma^*[k_p]$ . Then, denoting the noisy and noise-free intensity vectors by  $\vec{I}_n^* = [I_n^*[k_0] \cdots I_n^*[k_{M-1}]]^T$  and  $\vec{I}^* = [I^*[k_0] \cdots I^*[k_{M-1}]]^T$ , respectively, the log likelihood function is given as  $\log(p(\vec{I}_n^*|\tilde{k})) = -\frac{M}{2} \log(2\pi) - \frac{1}{2} \sum_{p=0}^{M-1} \log(\tilde{\sigma}_p^2) - (\vec{I}_n^* - \vec{I}^*)^T \cdot (\vec{I}_n^* - \vec{I}^*)$  where  $I_{n,\tilde{\sigma}}^*[k_p] \equiv I_n^*[k_p] / (\tilde{\sigma}_p \sqrt{2})$  and  $I_{\tilde{\sigma}}^*[k_p] \equiv I^*[k_p] / (\tilde{\sigma}_p \sqrt{2})$ . Fisher information matrix is given as follows:

$$I_F[\tilde{k}] \equiv E\left\{\left(\delta \log(p(\vec{I}_n^*|\tilde{k})) / \delta \tilde{k}\right)^2\right\} = -E\{\delta^2 \log(p(\vec{I}_n^*|\tilde{k})) / \delta \tilde{k}^2\} \quad (45)$$

where  $\delta(\cdot) / \delta \tilde{k}$  denotes the partial derivative of  $(\cdot)$  with respect to  $\tilde{k}$ . If the zero mean random variable is assumed at each sample point, then  $I_F[\tilde{k}]$  is obtained after simple calculations

as  $I_F[\tilde{k}] = \sum_{p=0}^{M-1} \tilde{\sigma}_p^{-2} (\delta I^*[k_p] / \delta \tilde{k})^2$  which depends on the square of the derivative of the intensity on the period  $\tilde{k}$ . Then, assuming an estimation method denoted by  $\tilde{k}$  has a bias  $b(\tilde{k}) \equiv E\{\tilde{k}\} - k$ , the Cramer-Rao Bound, i.e.,  $CR(\tilde{k})$ , satisfies  $\text{Var}(\tilde{k}) \geq CR(\tilde{k})$  for the variance of estimation where  $CR(\tilde{k})$  is given by the following:

$$CR(\tilde{k}) \equiv (1 + \delta b(\tilde{k}) / \delta \tilde{k})^2 / I_F[\tilde{k}] = (1 + \delta b(\tilde{k}) / \delta \tilde{k})^2 \left( \sum_{p=0}^{M-1} \tilde{\sigma}_p^{-2} (\delta I^*[k_p] / \delta \tilde{k})^2 \right)^{-1} \quad (46)$$

Furthermore, assuming  $\tilde{\sigma}_p^2 \leq \tilde{\sigma}_{max}^2$ , the maximum of the minimum variance bound is given by the following:

$$CR(\tilde{k}) \leq \tilde{\sigma}_{max}^2 (1 + \delta b(\tilde{k}) / \delta \tilde{k})^2 \left( \sum_{p=0}^{M-1} (\delta I^*[k_p] / \delta \tilde{k})^2 \right)^{-1} \quad (47)$$

while with  $\Delta G_2[n, l] \equiv \tilde{G}_2[l] - \tilde{G}_2[n]$ ,  $\delta I^*[k_p] / \delta \tilde{k}$  becomes as follows for  $I^*[k_p] \equiv I^G[k_p]$ :

$$\sum_{n=0}^{N_p-1} \sum_{l=0}^{N_p-1} g_{3,*}[n, l] g_{1,*}^{k_p}[n, l] g_{4,*}^{k_p^2}[n, l] e^{-\Delta G_2[n, l] i 2 \pi k_p / \tilde{k}} (\Delta G_2[n, l] i 2 \pi k_p / \tilde{k}^2) \quad (48)$$

and it is represented as follows for the normalized wave function  $I^*[k_p] \equiv e^{-2 A_{N-1} (k_p T_s)^2} I[k_p]$ :

$$\sum_{n=0}^{N_p-1} \sum_{l=0}^{N_p-1} g_{3,*}[n, l] g_{1,*}^{k_p}[n, l] e^{-\Delta G_2[n, l] i 2 \pi k_p / \tilde{k}} (\Delta G_2[n, l] i 2 \pi k_p / \tilde{k}^2) \quad (49)$$

## E Path Integral with Exotic Paths

The evolution of the wave function in  $n$ th path after the non-classical travels of  $k$  slits with  $k \in [1, N_E]$  as shown in Fig. 3 is given as  $\Psi_{n,j,k}^E(x_{j,k}^E) = \int_{x_j} f_{n,k}^E(x_{j,k}^E, x_j) \Psi_{n,j,0}^E(x_{j,0}^E) dx_j$  where  $\Psi_{n,j,0}^E(x_{j,0}^E) \equiv G_{n,j}(x_j - X_{j,s_{n,j}}) \Psi_{n,j}(x_j)$ ,  $x_{j,0}^E \equiv x_j$ ,  $f_{n,1}^E(x_{j,1}^E, x_j) \equiv K(x_{j,1}^E, t_{j,1}^E; x_j, t_j)$  and  $f_{n,k}^E(x_{j,k}^E, x_j)$  for  $k \geq 2$  is defined as follows:

$$\int_{\vec{x}_{j,k}^E} d\vec{x}_{j,k}^E K(x_{j,1}^E, t_{j,1}^E; x_j, t_j) \prod_{p=2}^k K(x_{j,p}^E, t_{j,p}^E; x_{j,p-1}^E, t_{j,p-1}^E) G_{n,j}(x_{j,p-1}^E - X_{j,s_{n,j,p-1}}) \quad (50)$$

while  $k = 0$  case corresponds to the wave function evolution without any non-classical path, i.e.,  $\Psi_{n,j,0}^E(x_{j,0}^E)$ ,  $t_{j,k}^E \equiv \sum_{p=1}^k t_{p-1,p}^E(j) + t_j$  is the time after visiting  $k$ th slit on  $j$ th plane,  $t_j$  corresponds to the time at the beginning of the non-classical movements and  $\vec{x}_{j,k}^E \equiv [x_{j,1}^E, x_{j,2}^E, \dots, x_{j,k-1}^E]$ . If it is assumed that the  $n$ th path performs  $k \geq 1$  consecutive visits to the slits on  $j$ th plane while the entrance slit is  $X_{j,s_{n,j}}$  and the wave function at the position  $x_j$  is  $\Psi_{n,j}(x_j)$ , then the wave function on the next plane, i.e.,  $\Psi_{n,j+1}(x_{j+1})$ , is calculated as follows:

$$\int K(x_{j+1}, t_{j,k}^E + t_{j,j+1}; x_{j,k}^E, t_{j,k}^E) G_{n,j}(x_{j,k}^E - X_{j,s_{n,j,k}}) \Psi_{n,j,k}^E(x_{j,k}^E) dx_{j,k}^E \quad (51)$$

**Acknowledgements** I would like to thank the referees for very helpful comments and suggestions.

## References

1. Feynman, R. P., Hibbs, A. R., Styer, D. F.: Quantum mechanics and path integrals. Dover Publications, New York, USA, emended edition (2010)
2. Puentes, G., La Mela, C., Ledesma, S., Iemmi, C., Paz, J. P., Saraceno, M.: Optical simulation of quantum algorithms using programmable liquid-crystal displays. *Phys. Rev. A*. **69**, 042319 (2004)
3. Vedral, V.: The elusive source of quantum speedup. *Foundations of Physics*. **40**, 1141 (2010)
4. Černý, V.: Quantum computers and intractable (NP-complete) computing problems. *Phys. Rev. A*. **48**, 116 (1993)
5. Haist, T., Osten, W.: An optical solution for the traveling salesman problem. *Optics Express* **15**, 10473 (2007)
6. Rangelov, A. A.: Factorizing numbers with classical interference: several implementations in optics. *Journal of Physics B: Atomic, Molecular and Optical Physics* **42**, 021002 (2009)
7. Aaronson S., Arkhipov, A.: The computational complexity of linear optics. In: Proc. of the Forty-third Annual ACM Symposium on Theory of Computing, 333 (2011)
8. Flamini, F., Spagnolo, N., Sciarrino, F.: Photonic quantum information processing: a review. *Reports on Progress in Physics* **82**(1), 016001 (2018)
9. Wang, H., Li, W., Jiang, X., He, Y. M., Li, Y. H., Ding, X., Chen, M. C., Qin, J., Peng, C. Z., Schneider, C., Kamp, M.: Toward scalable boson sampling with photon loss. *Phys. Rev. Lett.* **120**(23), 230502 (2018)
10. Gulbahar, B.: Quantum entanglement and interference in time with multi-plane diffraction and violation of Leggett-Garg inequality without signaling. [arXiv:1808.06477](https://arxiv.org/abs/1808.06477) (2018)
11. Feynman, R.P.: Quantum mechanical computers. *Foundations of Physics*. **16**(6), 507 (1986)
12. Bausch, J., Crosson, E.: Analysis and limitations of modified circuit-to-Hamiltonian constructions. [arXiv:1609.08571](https://arxiv.org/abs/1609.08571) (2016)
13. Tempel, D.G., Aspuru-Guzik, A.: The Kitaev-Feynman clock for open quantum systems. *New Journal of Physics* **16**(11), 113066 (2014)
14. Kitaev, A. Y., Shen, A., Vyalı, M. N., Vyalı, M. N.: Classical and quantum computation (Volume 47). American Mathematical Society, Providence, Rhode Island (2002)
15. Aharonov, D., Van Dam, W., Kempe, J., Landau, Z., Lloyd, S., Regev, O.: Adiabatic quantum computation is equivalent to standard quantum computation. *SIAM Review* **50**(4), 755, (2008)
16. daPaz, I. G., Vieira, C. H. S., Ducharme, R., Cabral, L. A., Alexander, H., Sampaio, M. D. R.: Gouy phase in nonclassical paths in a triple-slit interference experiment. *Phys. Rev. A*. **9**, 033621 (2016)
17. Sawant, R., Samuel, J., Sinha, A., Sinha, S., Sinha, U.: Nonclassical paths in quantum interference experiments. *Phys. Rev. Lett.* **113**, 120406 (2014)
18. Caha, L., Landau, Z., Nagaj, D.: Clocks in Feynman's computer and Kitaev's local Hamiltonian: Bias, gaps, idling, and pulse tuning. *Phys. Rev. A* **97**(6), 062306 (2018)
19. Griffiths, R. B.: *Consistent Quantum Theory*. Cambridge Univ. Press, Cambridge, UK (2003)
20. Griffiths, R. B.: Consistent histories and the interpretation of quantum mechanics. *Journal of Statistical Physics* **36**(1-2), 219 (1984)
21. Griffiths, R. B.: Consistent interpretation of quantum mechanics using quantum trajectories. *Phys. Rev. Lett.* **70**(15), 2201 (1993)
22. Cotler, J., Wilczek, F.: Bell tests for histories [arXiv:1503.06458](https://arxiv.org/abs/1503.06458) (2015)
23. Cotler, J., Wilczek, F.: Entangled histories. *Physica Scripta* **T168**, 014004 (2016)
24. Kocia, L., Huang, Y., Love, P.: Semiclassical formulation of the Gottesman-Knill theorem and universal quantum computation. *Phys. Rev. A*. **96**, 032331 (2017)
25. Tannor, D. J.: *Introduction to quantum mechanics: a time-dependent perspective*. University Science Books (2007)
26. Koh, D. E., Penney, M. D., Spekkens, R. W.: Computing quopit Clifford circuit amplitudes by the sum-over-paths technique. [arXiv:1702.03316](https://arxiv.org/abs/1702.03316) (2017)
27. Yuan, X., Zhou, H., Gu, M., Ma, X.: Unification of nonclassicality measures in interferometry. *Phys. Rev. A* **97**(1), 012331 (2018)

28. Knill, E., Laflamme, R., Milburn, G. J.: A scheme for efficient quantum computation with linear optics. *Nature* **409**(6816), 46 (2001)
29. Bartlett, S. D., Sanders, B. C.: Requirement for quantum computation. *Journal of Modern Optics* **50**(15-17), 2331 (2003)
30. Sasaki, M., Suzuki, S.: Multimode theory of measurement-induced non-Gaussian operation on wideband squeezed light: Analytical formula. *Phys. Rev. A* **73**(4), 043807 (2006)
31. Bartlett, S. D., Sanders, B. C.: Efficient classical simulation of optical quantum information circuits. *Phys. Rev. Lett.* **89**(20), 207903 (2002)
32. Lund, A. P., Laing, A., Rahimi-Keshari, S., Rudolph, T., O'Brien, J. L. and Ralph, T. C.: Boson sampling from a Gaussian state. *Phys. Rev. Lett.* **113**(10), 100502 (2014)
33. Hamilton, C. S., Kruse, R., Sansoni, L., Barkhofen, S., Silberhorn, C., Jex, I.: Gaussian boson sampling. *Phys. Rev. Lett.* **119**(17), 170501 (2017)
34. Rhode, P. P., Motes, K. R., Dowling, J. P.: Sampling generalized cat states with linear optics is probably hard. [arXiv:1310.0297](https://arxiv.org/abs/1310.0297) (2013)
35. Kruse, R., Hamilton, C. S., Sansoni, L., Barkhofen, S., Silberhorn, C., Jex, I.: A detailed study of Gaussian boson sampling. [arXiv:1801.07488](https://arxiv.org/abs/1801.07488) (2018)
36. Arkhipov, I. I., Barasiński, A., Svozilík, J.: Negativity volume of the generalized Wigner function as an entanglement witness for hybrid bipartite states. *Scientific Reports* **8**(1), 16955 (2018)
37. Siyouri, F., El Baz, M., Hassouni, Y.: The negativity of Wigner function as a measure of quantum correlations. *Quantum Information Processing*, **15**(10), 4237 (2016)
38. Dahl, J.P., Mack, H., Wolf, A., Schleich, W.P.: Entanglement versus negative domains of Wigner functions. *Phys. Rev. A* **74**(4), 042323 (2006)
39. Veitch, V., Ferrie, C., Gross, D., Emerson, J.: Negative quasi-probability as a resource for quantum computation. *New Journal of Physics* **14**(11), 113011 (2012)
40. Albarelli, F., Genoni, M. G., Paris, M. G., Ferraro, A.: Resource theory of quantum non-Gaussianity and Wigner negativity. [arXiv:1804.05763](https://arxiv.org/abs/1804.05763) (2018)
41. Raussendorf, R., Browne, D. E., Delfosse, N., Okay, C., Bermejo-Vega, J.: Contextuality and Wigner-function negativity in qubit quantum computation. *Phys. Rev. A* **95**(5), 052334 (2017)
42. Veitch, V., Wiebe, N., Ferrie, C., Emerson, J.: Efficient simulation scheme for a class of quantum optics experiments with non-negative Wigner representation. *New Journal of Physics* **15**(1), 013037 (2013)
43. Kenfack, A., Życzkowski, K.: Negativity of the Wigner function as an indicator of non-classicality. *Journal of Optics B: Quantum and Semiclassical Optics* **6**(10), 396 (2004)
44. Kowalewska-Kudłaszuk, A., Kalaga, J. K., Leoński, W.: Wigner-function nonclassicality as indicator of quantum chaos. *Phys. Rev. E* **78**(6), 066219 (2008)
45. Siyouri, F. Z.: Markovian and non-Markovian dynamics of non-classical correlations and Wigner function for GHZ-type coherent states. *International Journal of Theoretical Physics*, **58**(1), 103 (2019)
46. Quijandría, F., Strandberg, I., Johansson, G.: Steady-State generation of Wigner-negative states in one-dimensional resonance fluorescence. *Phys. Rev. Lett.* **121**(26), 263603 (2018)
47. Bennett, J. S., Bowen, W. P.: Rapid mechanical squeezing with pulsed optomechanics. *New Journal of Physics*, **20**(11), 113016 (2018)
48. Childs, A. M.: Universal computation by quantum walk. *Phys. Rev. Lett.* **102**(18), 180501 (2009)
49. Sansoni, L., Sciarrino, F., Vallone, G., Mataloni, P., Crespi, A., Ramponi, R. and Osellame, R.: Two-particle bosonic-fermionic quantum walk via integrated photonics. *Phys. Rev. Lett.* **108**(1), 010502 (2012)
50. Singh, S., Chandrashekar, C. M.: Interference and correlated coherence in disordered and localized quantum walk. [arXiv:1711.06217v2](https://arxiv.org/abs/1711.06217v2) (2018)
51. Jeong, H., Paternostro, M. and Kim, M.S.: Simulation of quantum random walks using the interference of a classical field. *Physical Review A*, **69**, 012310 (2004)
52. Goyal, S. K., Roux, F. S., Forbes, A., Konrad, T.: Implementation of multidimensional quantum walks using linear optics and classical light. *Phys. Rev. A* **92**(4), 040302 (2015)
53. Tang, H., Lin, X. F., Feng, Z., Chen, J. Y., Gao, J., Sun, K., Wang, C. Y., Lai, P. C., Xu, X. Y., Wang, Y., Qiao, L. F.: Experimental two-dimensional quantum walk on a photonic chip. *Science Advances* **4**(5), eaat3174 (2018)

54. Schreiber, A., Gábris, A., Rohde, P. P., Laiho, K., Štefaňák, M., Potoček, V., Hamilton, C., Jex, I., Silberhorn, C.: A 2D quantum walk simulation of two-particle dynamics. *Science*, 1218448 (2012)
55. Knight, P. L., Roldán, E., Sipe, J. E.: Quantum walk on the line as an interference phenomenon. *Phys. Rev. A* **68**(2), 020301 (2003)
56. Jeong, H., Paternostro, M., Kim, M. S.: Simulation of quantum random walks using the interference of a classical field. *Phys. Rev. A* **69**(1), 012310 (2004)
57. Qi, F., et al.: Experimentally simulating quantum walks with self-collimated light. *Scientific Reports* **6**, 28610 (2016)
58. Perets, H. B., Lahini, Y., Pozzi, F., Sorel, M., Morandotti, R., Silberberg, Y.: Realization of quantum walks with negligible decoherence in waveguide lattices. *Phys. Rev. Lett.* **100**(17), 170506 (2008)
59. Lovett, N. B., Cooper, S., Everitt, M., Trevers, M., Kendon, V.: Universal quantum computation using the discrete-time quantum walk. *Phys. Rev. A* **81**(4), 042330 (2010)
60. Venegas-Andraca, S. E.: Quantum walks: a comprehensive review. *Quantum Information Processing* **11**(5), 1015 (2012)
61. Ferrie, C.: Quasi-probability representations of quantum theory with applications to quantum information science. *Reports on Progress in Physics* **74**(11), 116001 (2011)
62. Deconinck, B., Heil, M., Bobenko, A., Van Hoeij, M. and Schmies, M.: Computing Riemann theta functions. *Mathematics of Computation* **73**(247), 1417 (2004)
63. Riemann, G. F. B.: Theorie der Abel'schen functionen. *Journal für reine und angewandte Mathematik* **54**, 101 (1857)
64. Mumford, D.: Tata lectures on theta. I. Birkhäuser Boston Inc., Boston, MA (1983)
65. Frauenthiener J., Jaber C., Klein C.: Efficient computation of multidimensional theta functions. [arXiv:1701.07486](https://arxiv.org/abs/1701.07486) (2017)
66. Osborne, A. R.: Nonlinear Ocean Wave and the Inverse Scattering Transform. *International Geophysics Series Volume 97*, Oxford, Academic Press (2002)
67. Wahls, S., Poor, H. V.: Fast numerical nonlinear Fourier transforms. *IEEE Transactions on Information Theory* **61**(12), 6957 (2015)
68. Nielsen, M. A., Chuang, I. L.: Quantum computation and quantum information. Cambridge University Press, New York, USA (2010)
69. Dowker H. F., Halliwell, J. J.: Quantum mechanics of history: The decoherence functional in quantum mechanics. *Phys. Rev. D.* **46**, 1580 (1992)
70. Ozaktas, H., Zalevsky, Z., Kutay, M. A.: The fractional Fourier transform with applications in optics and signal processing. John Wiley and Sons, Chichester, UK (2001)
71. Jacobi, C. G. J.: *Fundamenta Nova Theoriae Functionum Ellipticarum*. Königsberg (1829)
72. Lagarias, J. C.: The computational complexity of simultaneous diophantine approximation problems. In: *IEEE 23rd Annual Symposium on Foundations of Computer Science*, 32 (1982)
73. Zieliński T. P., Duda, K.: Frequency and damping estimation methods-an overview. *Metrology and Measurement Systems* **18**, 505 (2011)
74. DiVincenzo D., Terhal, B.: Decoherence: the obstacle to quantum computation. *Physics World* **11**, 53 (1998)